University of Illinois at Urbana-Champaign

ACRC

Air Conditioning and Refrigeration Center   A National Science Foundation/University Cooperative Research Center

Effects of Varying Fan Speed on a Refrigerator/Freezer System

A. R. Cavallaro and C. W. Bullard

ACRC TR-63   July 1994

Abstract

Air-side heat transfer correlations were developed to describe variable conductance models for the condenser and evaporator. Few experimentally estimated parameters described well the changes of refrigerant and air-side conditions over a wide range of steady-state operating conditions for the extensively instrumented test refrigerator. Existing empirical correlations that describe the difficult geometry of the heat exchangers were successful for the condenser, but not as successful for the evaporator. By relating dome and discharge temperature of the compressor with a linear fit, which could be accurately estimated if compressor manufacturers disclosed information for one more point other than the rating point and included the dome temperature, an experimentally estimated air-side heat transfer correlation described well the compressor for the same changes of refrigerant and air-side conditions.

Table of Contents

List of Figures

List of Tables

Nomenclature

A	area	$[\text{ft}^2]$
a	availability	$[\text{Btu/(hr·ft}^2\text{·°F)}]$
C	heat capacity ($\dot{m}c_p$)	$[\text{Btu/(hr·°F)}]$
c_p	specific heat	$[\text{Btu/(lbm·°F)}]$
D	tube diameter	$[\text{ft}]$
D_h	hydraulic diameter	$[\text{ft}]$
G	mass flux	$[\text{lbm/(hr·ft}^2\text{)}]$
g	acceleration of gravity	$[\text{ft/s}^2]$
I	irreversibility	$[\text{Btu/hr}]$
HP	power	$[\text{horse power}]$
h	heat transfer coefficient	$[\text{Btu/(hr·ft}^2\text{·°F)}]$
h_{fg}	heat of vaporization	$[\text{Btu/lbm}]$
k	thermal conductivity	$[\text{Btu/(hr·ft·°F)}]$
L	length	
$\dot{m}$	mass flow rate	$[\text{lbm/hr}]$
Pwr	power	$[\text{Btu/hr}]$
Q	heat transfer	$[\text{Btu/hr}]$
q"	heat flux through tube wall	$[\text{Btu/(hr·ft}^2\text{)}]$
RPM	motor speed	$[\text{rpm}]$
s	wall thickness	$[\text{ft}]$
T	temperature	$[\text{°F}]$
U	heat transfer conductance	$[\text{Btu/(hr·ft}^2\text{·°F)}]$
$\dot{V}$	volumetric airflow rate	$[\text{cfm}]$
v	velocity	$[\text{ft/s}]$
x	quality	

Subscripts

air	air-side parameter
air, indsp	air, inlet of desuperheating region (evaporator)
air, insp	air, inlet of superheating region (evaporator)
air, intp	air, inlet of two-phase region (evaporator)
air, mid	downstream inlet air (condenser)
air, outdsp	air, outlet of desuperheating region (evaporator)
air, outsp	air, outlet of superheating region (evaporator)
air, outtp	air, outlet of two-phase region (evaporator)
calc	calculated value
comp	entire compressor
cond	entire condenser
dis	discharge refrigerant (outlet of compressor)
dome	dome of compressor shell
dsp	desuperheating region
evap	entire evaporator
evapload	measurement of evaporator load
f	refrigerator

l	liquid	
m	mean tube parameter	
meas	measured value	
rate	as described by rate equations	
ref	refrigerant-side parameter	
ref, indsp	refrigerant, inlet of desuperheating region (evaporator)	
ref, insp	refrigerant, inlet of superheating region (evaporator)	
ref, intp	refrigerant, inlet of two-phase region (evaporator)	
ref,outsb	refrigerant, outlet of subcooling region (condenser)	
ref, 1	condenser inlet refrigerant	
ref, 2	two-phase refrigerant (condenser)	
s	isentropic	
sb	subcooled region	
shell	compressor shell	
sp	superheating region	
suc	suction refrigerant (inlet of compressor)	
t	theoretical parameter	
tp	two-phase region	
tp1	two-phase refrigerant parameter upstream of condenser fan	
tp2	two-phase refrigerant parameter downstream of condenser fan	
v	vapor	
z	freezer	

Symbols

Δ	difference	
δq	discrepancy in predicted irreversibility (compressor)	[Btu/hr]
ε	effectiveness	
f	friction factor	
L	length scale	[ft]
μ	viscosity	[lb·s/ft^2]
ρ	density	[lb/ft^3]
ν	kinematic viscosity	[ft^2/s]
χ_{tt}	Lockhart-Martinelli parameter	$[\left(\dfrac{r_v}{r_l}\right)^{0.5}\left(\dfrac{m_l}{m_v}\right)^{0.1}\left(\dfrac{1-x}{x}\right)^{0.9}]$

Dimensionless groups

Bo	Boiling number	[q/(G·h$_{fg}$)]
Nu	Nusselt number	[h·D/k]
Pr	Prandtl number	[c$_p$·μ/k]
Re	Reynolds number	[G·D/μ]

Chapter 1: Introduction

Energy standards and CFC phase-out have affected strongly the refrigerator-freezer industry. Flexible models which can simulate off-design conditions are necessary to study the introduction of new technologies and acceptable chemical substitutes.

Admiraal and Bullard (1993) developed a variable-conductance model that accounted for changes in heat transfer coefficients for different refrigerant flow characteristics. This is an improvement over constant-conductance models (e.g. Merriam et. al. (1993), Porter and Bullard (1993)). This variable conductance model is more flexible than the constant-conductance models because it can predict the performance of alternative refrigerants. It is also more accurate, and is therefore used for each zone of the evaporator and condenser.

Existing refrigerator simulation models documented in the public domain do not describe condenser and evaporator geometries and fail to account for changes in heat exchanger performance due to changes in airflow characteristics. The model described by Merriam et al. (1993) provides a user option having some of these capabilities, but the equations are not listed or described in the documentation. Heat exchanger geometry and airflow patterns are too complex to be modeled theoretically, so empirical data and correlations are required. This report describes an experimental program aimed at minimizing the number of empirical parameters required to specify variable conductance models for the evaporator and the condenser of a typical 18 ft^3 refrigerator-freezer.

The test refrigerator is extensively instrumented on the air and refrigerant sides of each component as described in earlier publications (Reeves and Bullard (1994)). Admiraal and Bullard (1993) demonstrated that airflow rates and air-side heat transfer coefficients could be reliably estimated from only a few data points, for constant-speed fans. In fact, the single air-side heat transfer coefficient was estimated more easily than the several parameters required to specify a less versatile multi-zone constant-conductance model.

In this paper correlations for air-side heat transfer coefficients are determined experimentally with the variable-speed fans on both the evaporator and condenser. It is shown that such results can be easily applied to predict component and system performance. Resulting improvements in the system simulation model will permit assessments of the system performance impacts of varying airflow rates in addition to such other parameters as heat exchanger area.

References

Admiraal, D.M., and Bullard, C.W., *Heat Transfer in Refrigerator Condenser and Evaporators*, ACRC TR-48, Air Conditioning and Refrigeration Center, University of Illinois at Urbana-Champaign, 1993.

Merriam, Richard, Varone, A., and Feng, H., EPA *Refrigerator Analysis Program User Manual,* Version 1.0, Arthur D. Little, Inc., 1993.

Porter, K.J., and Bullard, C.W., *Modeling and Sensitivity Analysis of a Refrigerator/Freezer System*, ACRC TR-31, Air Conditioning and Refrigeration Center, University of Illinois at Urbana-Champaign, 1992.

Reeves, R.N., Bullard, C.W., and Crawford, R.R., *Measurement of Refrigerator Component Performance*, ASHRAE Transactions, 100:1, 1335-1343, 1994.

Chapter 2: Evaporator and condenser variable conductance

2.1 Overall heat transfer coefficients

The overall heat transfer coefficient is a function of refrigerant-side, air-side, and condenser wire and tube conductances:

$$\frac{1}{U_t\,A_t} = \frac{1}{h_{ref}\,A_{ref}} + \frac{s}{k\,A_m} + \frac{1}{h_{air}\,A_{air}} \tag{2.1}$$

where U_t, h_{ref}, h_{air} are respectively the overall, refrigerant-side, and air-side heat transfer coefficients, k is the conductivity of the heat exchanger material, A_t, A_{ref}, A_{air}, A_m are the overall, refrigerant-side, air-side, and mean surface areas, and s is the thickness of the heat exchanger.

By omitting the negligible resistance of the heat exchanger materials, and by normalizing overall heat transfer coefficient to the outside surface area, the equation reduces to

$$\frac{1}{U_t} = \frac{A_{air}}{h_{ref}\,A_{ref}} + \frac{1}{h_{air}} \tag{2.2}$$

This equation applies to each zone of the evaporator and condenser. Appropriate refrigerant-side and air-side heat transfer coefficients are estimated and applied to each zone.

2.2 Refrigerant-side heat transfer correlations

The refrigerant-side heat transfer correlations can predict the performance of current and alternative refrigerants, unlike constant-conductance models which are valid for only a single refrigerant. These correlations were validated in the test refrigerator by Admiraal and Bullard (1993). The single-phase correlation used in the subcooled and superheated regions is the Gnielinsky (Incropera and De Witt, 1990):

$$Nu_D = \frac{(f/8)\cdot(Re_D - 1000)\cdot Pr}{1 + 12.7\cdot(f/8)^{0.5}\cdot(Pr^{2/3} - 1)} \tag{2.3}$$

where the friction factor f for smooth tubes is

$$f = (0.79\cdot\ln Re_D - 1.64)^{-2} \tag{2.4}$$

This correlation is valid for $0.5 < Pr < 2000$ and $10^4 < Re_D < 5\text{x}10^6$.

The two-phase correlation used for condensation is from Dobson et al. (1994):

$$h_{tp} = f(c_{tt})\cdot\left[\frac{(r_l\cdot(r_l - r_v)\cdot g\cdot h_{fg}\cdot k_l^3)}{(D\cdot\Delta T\cdot m_l)}\right]^{0.25} \tag{2.5}$$

and

$$f(c_{tt}) = \frac{0.375}{c_{tt}^{0.23}} \tag{2.6}$$

where the Lockhart and Martinelli (1949) parameter c_{tt} is

$$c_{tt} = \left(\frac{r_v}{r_l}\right)^{0.5} \left(\frac{m_l}{m_v}\right)^{0.1} \left(\frac{1-x}{x}\right)^{0.9}$$

(2.7)

Quality varies from saturated vapor to liquid. With the assumption of constant heat flux over the whole condensing area, an average two-phase heat transfer coefficient is calculated by integrating over the quality span in the two-phase region. Since the two-phase correlation is not valid as the quality approaches 0 and 1, it is approximated by only integrating between a quality of 0.05 to 0.95. The result of integrating the $\left(\frac{1-x}{x}\right)^{0.9}$ term is 1.77, which is different from the 0.138 local value (x=0.9) used by Admiraal and Bullard (1993). Using either value, though, does not affect significantly the prediction of the overall heat transfer coefficient, since the refrigerant-side heat transfer coefficient of the two-phase region is much larger than the air-side coefficient.

The two-phase correlation used for evaporation from Wattelet et al. (1994):

$$h_{tp} = h_l \left(4.3 + 0.4 \, (Bo \, 10^4)^{1.3} \right)$$

(2.8)

where

$$Bo = \frac{q''}{G \, h_{fg}}$$

(2.9)

$$h_l = 0.023 \, Re_l^{0.8} \, Pr_l^{0.4} \frac{k_l}{D}$$

(2.10)

2.3 Air-side heat transfer correlations

The air-side heat transfer coefficient used for all of the regions of the condenser and evaporator is

$$h_{air} = \frac{Nu \cdot k}{L}$$

(2.11)

where the Nusselt number is correlated using the following algebraic expression

$$Nu = r \cdot Re^m \cdot Pr^n$$

(2.12)

and

$$Re = \frac{v \cdot L}{v}$$

(2.13)

$$Pr = \frac{\mu \cdot c_p}{k}$$

(2.14)

In this set of equations Re is the Reynolds number, Pr is the Prandtl number, μ is the viscosity, v is the kinetic viscosity, k is the conductivity, v is the velocity, c_p is the specific heat of the air, and L is the length scale. The parameters r, m, and n are dependent on the flow regime and on the geometry of the heat exchanger.

2.3.1 Empirical correlations for the evaporator

Heat transfer to the evaporator tubes and fins are calculated separately. The tubes are modeled as a bank of cylinders in cross flow, using the Zhukauskas correlation for forced convection:

$$Nu = 0.51 \cdot Re_D^{0.5} \cdot Pr^{0.36}$$

(2.15)

3

for $10^2 < Re_D < 10^3$ (Incropera and De Witt, 1990), using the tube diameter as length scale. During testing, the Reynolds number ranged between 400 and 930. Coincidentally, in this particular range of Reynolds numbers the correlation for the bank of tubes is identical to that for a single isolated cylinder. Since the number of rows is less than 20 cylinders, a correction factor, suggested by Zhukauskas, is applied to the Nusselt number (Incropera and De Witt, 1990):

$$Nu_{(rows=6)} = 0.93 \cdot Nu \qquad (2.16)$$

Flow between the fin plates is modeled as channel flow between isothermal parallel plates using Stephan's correlation (Shah and Bhatti, 1987) for forced convection:

$$Nu = 7.55 + \frac{0.024 \cdot \left(\dfrac{L}{D_h \cdot Re_{D_h} \cdot Pr} \right)^{-1.14}}{1 + 0.0358 \cdot Pr^{0.17} \left(\dfrac{L}{D_h \cdot Re_{D_h} \cdot Pr} \right)^{-0.64}} \qquad (2.17)$$

where the hydraulic diameter D_h is twice the spacing between parallel plates. For the range of tested air velocities (1.8 to 4.2 ft/s) the air-side heat transfer coefficient of the fin plates varies with air velocity is to the 0.67 power.

In the limiting case of a shorter fin length, a wider hydraulic diameter, or a higher air velocity, the unity term in the denominator becomes insignificant, and the power dependence of the correlation is to the 0.5 power. This exponent is identical to the one of the correlation for laminar flow over a flat plate since the boundary-layers of the parallel fins do not meet. The other limiting case requires a longer length, a narrower hydraulic diameter, or a slower velocity. Then the heat transfer coefficient varies with velocity to the 1.14 power.

The heat transfer coefficients of tubes and fin plates are weighted using their surface areas:

$$h_{air,evap} = \frac{h_{air,plates} \cdot A_{plates} + h_{air,tubes} \cdot A_{tubes}}{A_{plates} + A_{tubes}} \qquad (2.18)$$

where the surface area of the plates makes up 74.8% of the total surface area. Since the heat transfer coefficient for the tube section is slightly larger than for the plates, the weighted heat transfer coefficient of the plates accounts for 70% of the total air-side heat transfer coefficient. The overall dependence of the air-side heat transfer coefficient on air velocity is to the 0.64 power.

2.3.2 Empirical and theoretical correlations for the condenser

Heat transfer to the condenser tubes and wires are calculated separately. The wire fins are modeled as cylinders in cross flow, using diameter as the length scale. Zhukauskas correlation for forced convection over a cylinder is

$$Nu = 0.51 \cdot Re_D^{0.5} \cdot Pr^{0.36} \qquad (2.19)$$

for $40 < Re_D < 1000$ (Incropera and De Witt, 1990). Reynolds number ranged between 65 and 275 during testing.

The tubes, which are oriented parallel to the airstream, are modeled as flat plates having the width equal to the circumference of the tube. The theoretical laminar-flow correlation is

$$Nu = 0.664 \cdot Re_L^{0.5} \cdot Pr^{0.36} \qquad (2.20)$$

for $Re_L < 5 \times 10^5$ (Incropera and De Witt, 1990). During testing, the Reynolds number ranged between 0.9×10^5 and 3.7×10^5.

Once the heat transfer coefficients are estimated separately for wires and tubes, they are weighted with the fraction of the area of the wires and tubes:

$$h_{air,cond} = \frac{h_{air,wires} \cdot A_{wires} + h_{air,tubes} \cdot A_{tubes}}{A_{wires} + A_{tubes}} \qquad (2.21)$$

where the surface area of the wires covers 51.5% of the total surface area. Since the heat transfer coefficient is larger for the wire section than for the tube section, the weighted heat transfer coefficient of the wire accounts for 91% of the total air-side heat transfer coefficient. The overall dependence of the air-side heat transfer coefficient on air velocity is therefore expected to be to the 0.5 power, since it is the same for the wires and the tubes.

2.3.3 Experimental correlation for condenser and evaporator

Both the condenser and the evaporator are made up of fins and tubes, which have completely different length scales and independent air-side heat transfer correlations. Because of the complex geometry and the impossibility of defining a single length scale, the experimental air-side correlation is expressed in its dimensional form, which, unfortunately, is not as general as the dimensionless Equation 2.14. Air conductivity, specific heat, and viscosity are assumed constant since including them would affect by less than 1% the accuracy of air-side heat transfer coefficient calculations for our range of test conditions. The simplified air-side heat transfer correlation is

$$h_{air} = c \cdot v^m \qquad (2.22)$$

where the coefficient c and exponent m are determined experimentally with the Fall '93 data set for the condenser and with the Spring '94 data set for the evaporator. These two data sets were taken with the same test refrigerator: the fan speed was varied in the condenser for the Fall '93 data set and in the evaporator for the Spring '94 data set.

2.4 Evaporator results

Evaporator air-side heat transfer coefficients for both experimental and general (Zhukauskas and Stephan) correlations are displayed in Figure 2.1. The overall heat transfer coefficient for the general correlation is not as sensitive to velocity changes as for the experimental correlation. Stephan's empirical correlation for channel flow between parallel plates, which accounts for 70% of the heat transfer of the evaporator, is insensitive to air velocity. A physical explanation for the shortcoming of the Stephan's empirical correlation is that vorticies from the tubes and the slightly bent shape of the fins could augment turbulence and heat transfer, especially at higher velocities.

In these experimental heat transfer calculations contact resistance and fin effectiveness are neglected. According to O'Neill (1987), though, contact resistance could account up to 25% of the total resistance for a similar evaporator. If this were true for our test evaporator, the experimentally estimated air-side heat transfer coefficient would have to be larger and the disagreement between theoretical and experimental results would be accentuated. On the other hand, it is safe to assume that the effectiveness of the actual fin is near unity, since, according to O'Neill (1987), the thickness of the fin did not seem to affect the effectiveness of the evaporator.
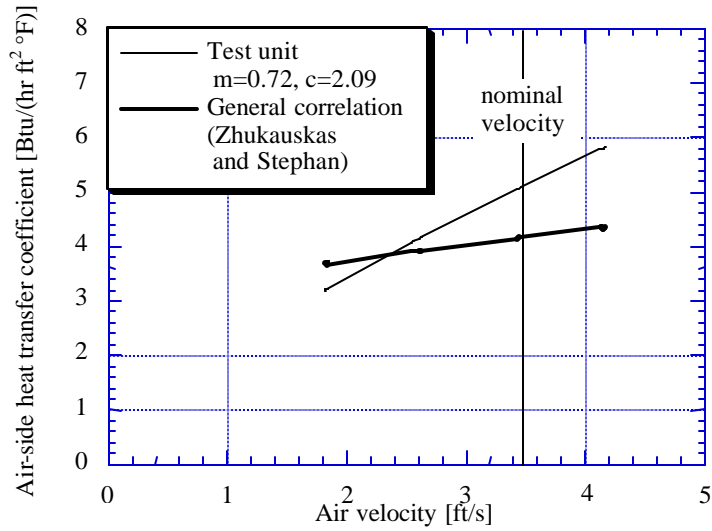
Figure 2.1 Evaporator air-side heat transfer coefficients

In Figure 2.2, the experimental correlation estimates convective heat transfer with a precision interval of 22 Btu/hr, while the general correlations of Zhukauskas and Stephan predict the measured data with a precision interval of 92 Btu/hr. The precision interval is defined by $|\mu| + 2\sigma$, where μ is the bias mean deviation from the predicted value and σ is the standard deviation of each point from the mean. Assuming a Gaussian error distribution, 95% of the data points lie within 2σ of the mean.

Figure 2.2 shows that predicted heat transfer from the general correlations (Zhukauskas and Stephan) is arranged in several clusters that cross the measured convective heat transfer line. Each cluster represents a different evaporator inlet air temperature setting, and the variation within each cluster is attributable to changes in air velocity. It is evident that the experimental results do a good job in predicting heat transfer as a function of velocity, while the general ones do not.
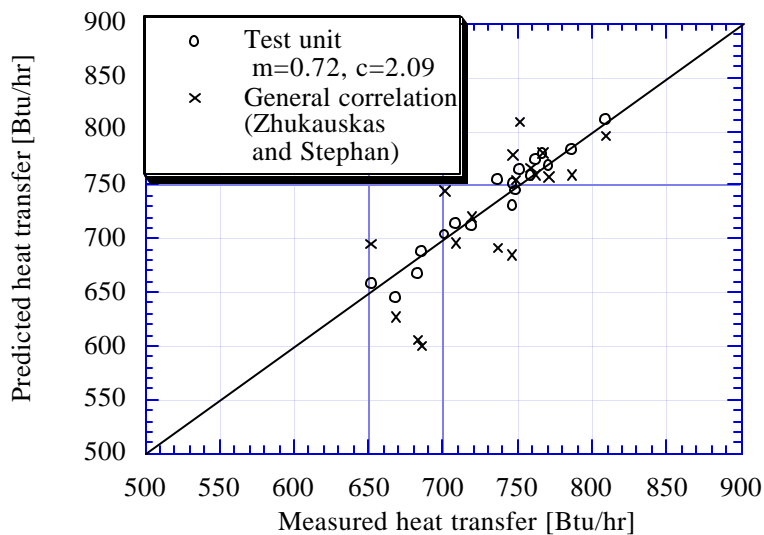
Figure 2.2 Predicted evaporator heat transfer

When implementing the equations that describe the evaporator in a system model, it is important not only to estimate accurately the convective heat transfer, but also the outlet refrigerant conditions. In design models such as those developed by ADL (1982) and Merriam et al. (1993) the evaporator outlet conditions must be specified by the user. In the ACRC simulation model, however, it is calculated, and errors may propagate throughout the refrigerator system model. Figure 2.3 shows how both experimental and general correlations predict outlet conditions. All 18 data points were taken with a superheat outlet condition, but some of the predictions indicate a two-phase outlet condition at the quality shown.

In estimating the empirical parameters, and in predicting convective heat transfer, the refrigerant-side pressure drop across the evaporator is assumed to be negligible. Measured outlet pressure and inlet temperatures are used to predict the outlet temperature. Since the pressure drop across the evaporator was always less than 0.5 psi, the prediction of superheat could be affected by only 0.5°F in the worse case.
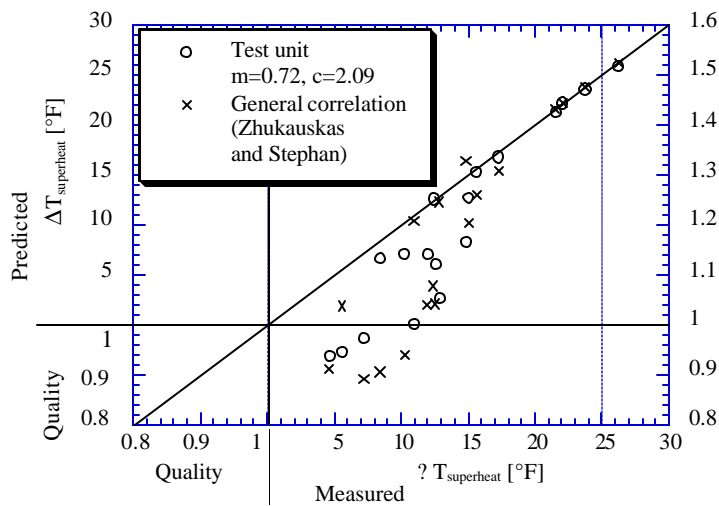
Figure 2.3 Predicted evaporator outlet conditions: degrees of superheat or quality

2.5 Condenser results

Condenser airflow rate and heat transfer coefficient estimates of Admiraal and Bullard (1993) and Reeves and Bullard (1992) had many uncertainties due to numerous air-side complexities. Therefore, a calorimeter approach, which gave better air-side measurements and made the modeling of the condenser cabinet much easier, was used. This involved modifying the condenser cabinet in such matter that all of the openings other then grill inlet and outlet were sealed with duct tape, a partition was installed to prevent recirculation of outlet air, and the front grille was removed to obtain data over the widest range of velocities (Appendix C). With this calorimeter setup the airflow rate at the nominal speed was 158 cfm.

Condenser air-side heat transfer coefficients for both the experimental and empirical (Zhukauskas and flat plate) correlations agree very well with one another, as shown in Figure 2.4. Since the experimental exponent m = 0.53 agrees so well with the empirical one m = 0.5, it would be possible to estimate the parameter c from a single data point (i.e. at the nominal fan speed) by setting the exponent to the empirically accepted m = 0.5.
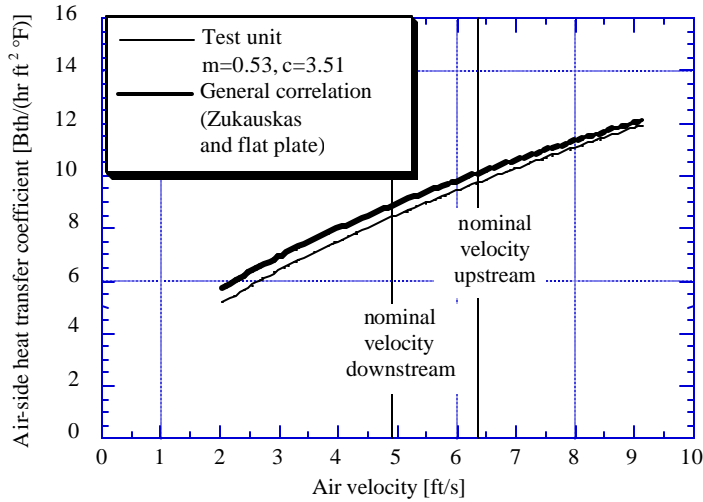
Figure 2.4 Condenser air-side heat transfer coefficients

In Figure 2.5, experimental results predict well condenser convective heat transfer accurately. In these calculations, the refrigerant-side pressure drop across the condenser is neglected. Goodson (1994) predicts a pressure drop of 1 psi across the condenser, of which about 75% is in the two-phase region. The observed pressure drop across the condenser was 2 psi, but it is believed that 1 psi is caused by the mass flow meter at the exit of the condenser. This pressure drop across the condenser would translate into errors less than 0.1°F in estimating the amount of subcooling, less than 0.3°F in predicting the saturation temperature, and less than 0.4°F in computing the amount of superheat. These errors are not significant relative to the uncertainty of the thermocouples.

A better test of the condenser model is its ability to predict subcooling, which affects mass flow through the capillary tube, so errors will propagate through the rest of the system model. In Figure 2.6, predictions based on the test unit correlation and general correlations for a flat plate and cylinder in cross flow predict well the outlet refrigerant temperature. The data showed subcooling for all points, but some of the predictions indicate a two-phase outlet condition at the quality shown.
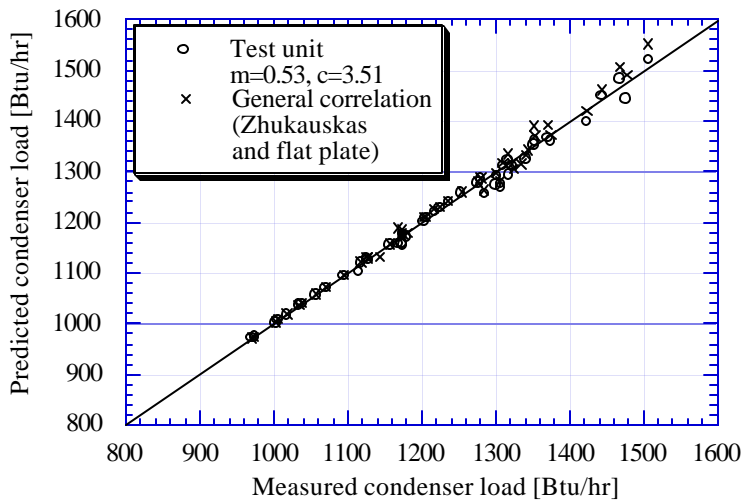
Figure 2.5 Predicted condenser heat transfer
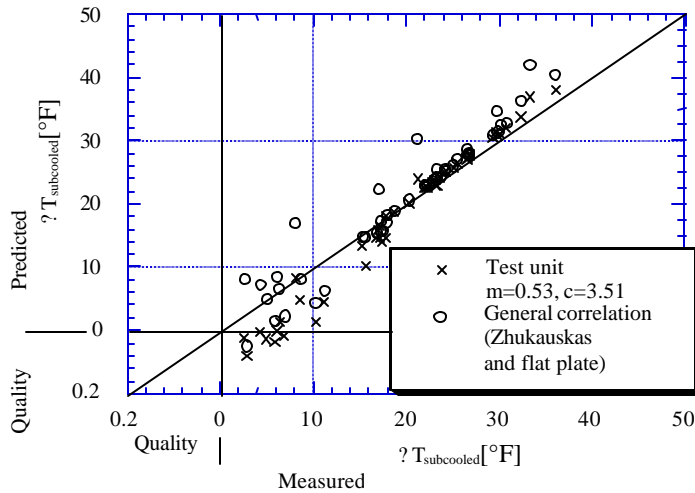
Figure 2.6 Predicted condenser outlet condition: degrees of subcooled or quality

References

Admiraal, D.M., and Bullard, C.W., *Heat Transfer in Refrigerator Condenser and Evaporators*, ACRC TR-48, Air Conditioning and Refrigeration Center, University of Illinois at Urbana-Champaign, 1993.

Coulter, W. H., personal communication, University of Illinois, Urbana, IL, 1994.

Dobson, M. K., Chato, J. C., et al., *Heat Transfer and Flow Regimes During Condensation in Horizontal Tubes*, ACRC TR-57, Air Conditioning and Refrigeration Center, University of Illinois at Urbana-Champaign, 1994.

Goodson, M. P., personal communication, University of Illinois, Urbana, IL, 1994.

Icropera, F. P., and De Witt, D. P., *Fundamentals of Heat and Mass Transfer*, 3rd ed., John Wiley & Sons, Inc., New York, 1990.

Lockhart, R.W., and Martinelli, R.C., "Proposed Correlation of Data for Isothermal Two-phase Two-Component Flow in Pipes," *Chemical Engineering Progress*, Vol. 45 No. 1, 1949.

Merriam, Richard, Varone, A., and Feng, H., EPA *Refrigerator Analysis Program User Manual,* Version 1.0, Arthur D. Little, Inc., 1993.

O'Neill, P. J., Crawford, R. R., Thermal Performance Analysis of Finned Tube Heat Exchangers at Low Temperatures and Airflow Rates, ASHRAE Transactions 3162, Vol. 94 Part 2, 1988.

Reeves, R.N., Bullard, C.W., and Crawford, R.R., *Modeling and Experimental Parameter Estimation of a Refrigerator/Freezer System*, ACRC TR-9, Air Conditioning and Refrigeration Center, University of Illinois at Urbana-Champaign, 1992.

Shah, R.K., and Bhatti, M.S., "Laminar Convective Heat Transfer in Ducts," *Handbook of Single-Phase Convective Heat Transfer*, Wiley & Sons, Inc., New York, 1987.

Wattelet, J.P., Chato, J. C., et al., *Heat Transfer Flow Regimes of Refrigerants in a Horizontal-Tube Evaporator* ACRC TR-55, Air Conditioning and Refrigeration Center, University of Illinois at Urbana-Champaign, 1994.

Chapter 3: Compressor convective heat transfer

3.1 Convective heat transfer correlation

In the previous chapter, variable-conductance models were used to describe the evaporator and the condenser for different operating conditions. When simulating the whole refrigerator/freezer system at a variable condenser fan speed, the compressor must also be described in terms of the airflow characteristics.

Rubas and Bullard (1993) determined the compressor air-side heat transfer coefficient at the nominal airflow rate by calculating the slope between the compressor heat load, and the shell to air temperature difference. They encountered small scatter and no bias. Their results were obtained at a constant airflow rate. At variable fan speeds, though, the air-side heat transfer coefficient will vary with air velocity:

$$h_{air,comp} = c \cdot v^m \tag{3.1}$$

as in the case of the condenser and compressor variable-conductance models. Since the compressor is located 4 inches downstream of the fan, the air velocity over the compressor is approximated by dividing airflow rate by the cross-sectional area of the fan.

Shell temperature is the theoretically correct parameter to describe the temperature difference between the compressor and the fluid in the convective heat transfer equation. The modeler, though, is left without a relationship linking shell temperature, which is not a parameter already existing in the model, to any other variables which are modeled. ADL (1982) and Merriam (1993) overcame this problem by assuming that the driving temperature difference was (T_{dis} - T_{air}) instead of (T_{shell} - T_{air}); where T_{shell} is the surface shell temperature, T_{dis} is the refrigerant-side discharge temperature, and T_{air} is the air temperature. Since this crude approximation has no theoretical basis, experiments were conducted to examine the relationship between discharge and shell temperatures, so that the appropriate form of the convective heat transfer equation can be used.

3.2 Use of rating point data

The Fall '93 data set, which was used to determine the air-side heat transfer coefficients of the condenser, is also used for the compressor analysis. This experiment was conducted with four surface thermocouples (Appendix F) which had a constant gradient of 30°F. Since the dome temperature was near the arithmetic average of these thermocouples, it is used to approximate the average shell temperature and to describe the temperature difference between the compressor and the fluid.

The relationship between dome and discharge temperature was found to be linear:

$$T_{dome} = 0.855 \cdot T_{dis} - 24.7 \tag{3.2}$$

where the units are in degrees Fahrenheit. To determine the two parameters (slope and intercept) of this equation it is not necessary to have a large data set as the one used in Appendix F; rather it would be sufficient that the compressor manufacturers provided the discharge and dome temperature for one point other than the rating point.

The parameter c of Equation 3.1 was estimated at the rating point conditions by assuming that the empirical exponent m = 0.5, corresponding to a flat plate or spherical geometry. For comparison, the parameters c and m were estimated to give the best agreement between predicted and measured heat transfer for the Fall '93 data set. In Figure

3.1, these two estimates are compared to one another. The experimental heat transfer coefficient obtained at the rating point is only 2.5% smaller than the heat transfer coefficient estimated from the complete 48-point data set.

Figure 3.2 shows that predictions of compressor heat loss lie within 10% of the measured values. The precision interval of predicted heat transfer for the experimental results is 19.9 Btu/hr, while for the rating point results it is 28.4 Btu/hr. The heat transfer prediction based on the rating point has about the same amount of scatter as the experimental results, but with a larger bias.
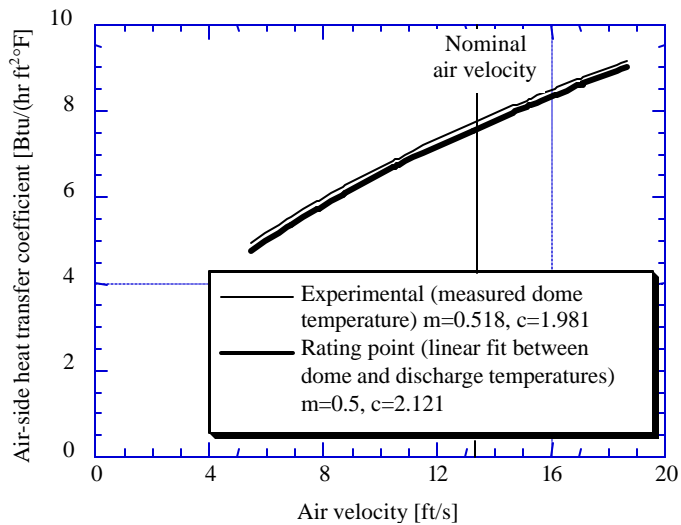
Figure 3.1 Compressor air-side heat transfer coefficients
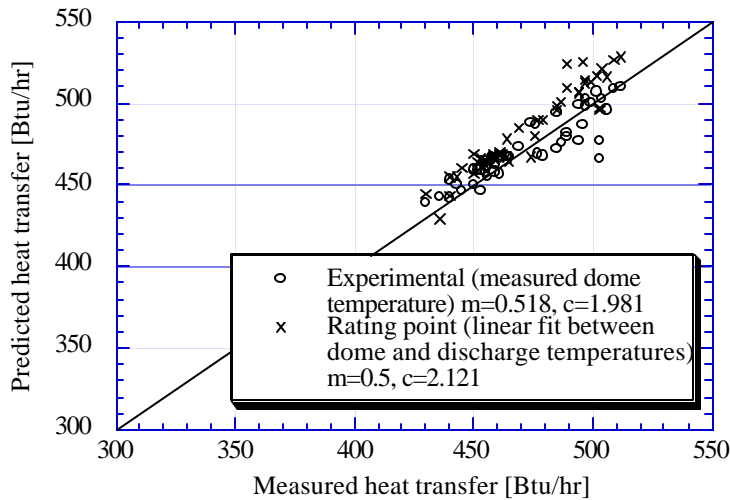
Figure 3.2 Predicted compressor heat transfer

3.4 Compressor simulation

The parameter estimation is completed, so the estimated parameters obtained from the rating point conditions will be used to simulate the compressor for given inlet refrigerant and air-side conditions. In a compressor model the refrigerant mass flow rate and power maps are used to determine discharge pressure and input power for

given inlet refrigerant and air-side conditions. The inaccuracy of the maps can cause significant propagation of error, not only at the component level, but also at a system level.

Figure 3.3 shows that the model overpredicts discharge temperature for all of the 48 conditions by approximately 20°F. This is caused by the inaccuracy of the refrigerant mass flow rate map in which large changes in condensing temperature have only a small effect on mass flow rate, so small errors modeling mass flow rate can affect significantly the modeled condensing temperature and pressure. This might not be the case for another compressor.

In Figure 3.4, the variance in the predicted heat transfer is due to the uncertainty of the estimated heat transfer coefficient, and is skewed because of the offset in estimating the compressor power with the map (Appendix E).
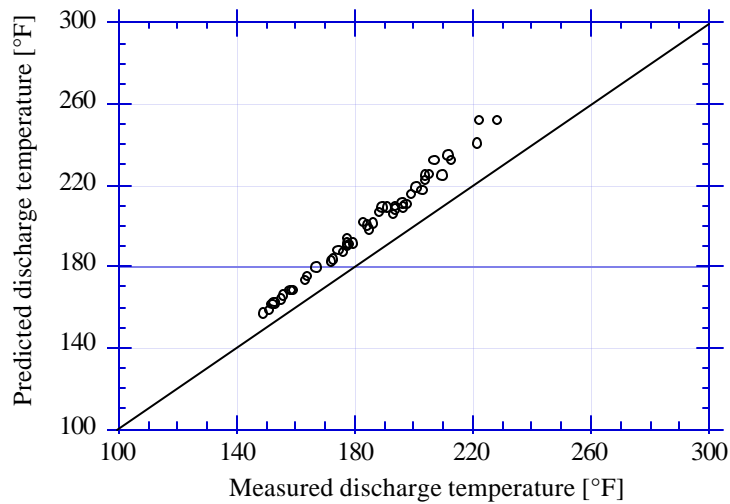
Figure 3.3 Predicted discharge temperature with compressor map
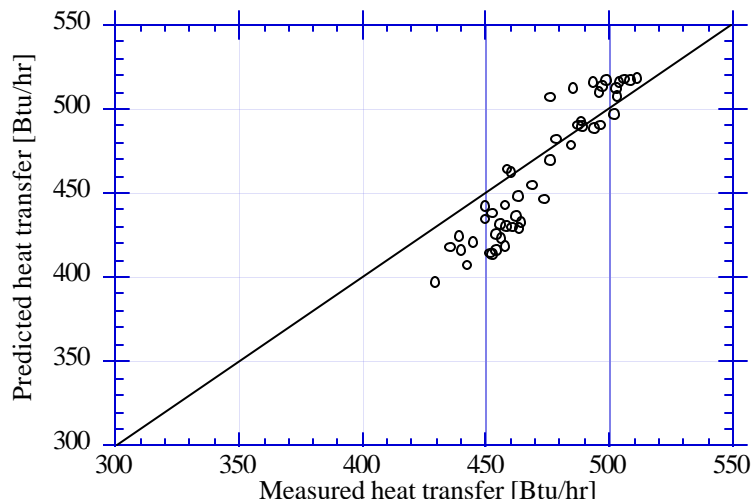
Figure 3.4 Predicted heat transfer with compressor map

References

Admiraal, D.M., and Bullard, C.W., *Heat Transfer in Refrigerator Condenser and Evaporators*, ACRC TR-48, Air Conditioning and Refrigeration Center, University of Illinois at Urbana-Champaign, 1993.

Arthur D. Little, Inc. *Refrigeration and Freezer Computer Model User's Guide*, U.S. Department of Energy, Washington D.C., 1982.

Merriam, Richard, Varone, A., and Feng, H., EPA *Refrigerator Analysis Program User Manual,* Version 1.0, Arthur D. Little, Inc., 1993.

Rubas, P. J., Bullard, C. W., *Assessments of Factors Contributing to Refrigerator Cycling Losses*, ACRC TR-45, Air Conditioning and Refrigeration Center, University of Illinois at Urbana-Champaign, 1993.

Chapter 4: Summary and recommendations

Variations in heat transfer coefficients resulting from changes in refrigerant and air-side conditions were described using variable-conductance models. Air velocities spanned a factor of two in the evaporator and a factor of three in the condenser cabinet. The attempt to describe air-side heat transfer coefficients with a small number of experimentally estimated parameters was successful: the experimental correlation for the condenser predicted heat transfer within ±3%; and the experimental correlation for the evaporator predicted heat transfer within ±4% for large sets of measured data.

Fundamental correlations from literature were applied to the complex geometry of the wire and tube condenser, which was subject to a uniform airflow: predicted heat transfer was within ±3%, thus as good as the best fit of the data. Fundamental correlations were not as successful in predicting the evaporator heat transfer, where the scatter was ±13%.

Results obtained at variable fan speeds not only demonstrated the success of describing the air-side heat transfer coefficients, but also validated the refrigerant-side heat transfer correlations.

The compressor heat transfer correlation obtained using only the rating point data (±6%) was almost as good as the one obtained by using the complete data set (±5%). The relation between discharge and dome temperature was linear, and could be easily estimated if compressor manufacturers would publish dome and discharge temperatures at one point in addition to the rating point. Providing this additional information would not require much additional effort. It is not known whether the relationship between dome and discharge temperature is linear for other compressors.

The ability to estimate accurately the air-side parameters for the condenser is attributed to the calorimeter setup, which simplified many, but certainly not all of the air-side complexities. Now that the air-side heat transfer correlation is known for the calorimeter setup, it would be interesting to relate it to the original setup which has numerous openings and airflow complexities.

The need to have superheat at the outlet of the evaporator to estimate an accurate refrigerant mass flow rate might have prevented the calculation of a more accurate air-side heat transfer correlation for the evaporator. If manufacturer's refrigerant mass flow rate maps could have been trusted completely, it would have been possible to operate the evaporator with a two-phase outlet condition, which would have simplified determination of the air-side heat transfer correlation. Possibly, a new and more accurate mass flow rate map should be developed for this compressor, using the data obtained here. Also, the mass flow rate meter should be recalibrated after having been clogged and cleaned several times, but it is only useful when the condenser outlet is subcooled.

The small desuperheating tube and accumulator located downstream of the evaporator made the prediction of the refrigerant outlet temperature and the parameter estimation of the air-side heat transfer coefficient difficult. A surface thermocouple mounted right at the exit of the evaporator might eliminate the need to predict desuperheating, which would improve the confidence of the results.

In both the evaporator and condenser cabinet, the upper limit for airflow rate was set by the power rating of the fan motor and frequency controller. New technologies have brought ECM (Electronically Commutated Motors) which can easily vary fan speed and possibly permit much higher airflow rates over the condenser and evaporator. A wider range of airflow rates would improve the experimental estimation of the two parameters c and m in Equation 2.22.

Appendix A: Evaporator geometry and airflow rate measurement

Airflow rate through the evaporator is made up of two streams which travel through the refrigerator and freezer compartments. These two separate streams return from the freezer and refrigerator, and mix into a single stream which is the evaporator air inlet temperature:

$$T_{air,in} = f_z T_z + (1 - f_z) T_f \qquad\qquad (A.1)$$

where $T_{air,in}$ is the evaporator inlet temperature, T_z and T_f are the freezer and refrigerator return temperatures, and f_z is the fraction of air that travels through the freezer. Then the mixed air flows over the evaporator as shown in Figure A.1.
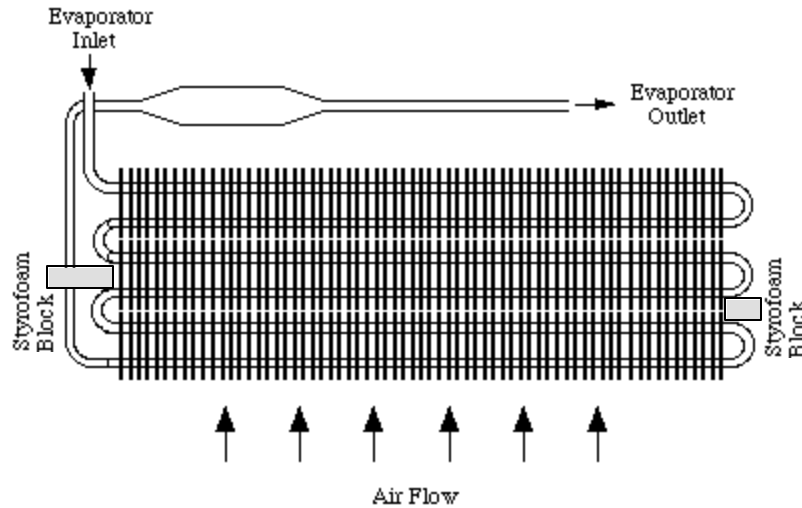
Figure A.1 Evaporator counter flow geometry

Airflow rate is calculated with the energy balance

$$C_{air} (T_{air,out} - T_{air,in}) = Q_{load} \qquad\qquad (A.2)$$

where $T_{air,out}$ is the temperature of the air past the evaporator, and Q_{load} is the evaporator load.

Admiraal and Bullard (1993) estimated for the Fall '92 data set a flow rate of 66 cfm with an 85% airsplit fraction, and for the Spring '93 data set a flow rate of 69 cfm with an 86% airsplit fraction. In the Fall '93 data set, however, the flow rate was found to be 72 cfm and the airsplit fraction was 87%. Airflow rate disagreement between different data sets could have been caused by changes to the evaporator cabinet during instrumentation. Between the Spring '93 and the Fall '93 data sets, the evaporator cabinet was opened to install a microphone. Airflow characteristics or the location of certain air side thermocouples could have been affected.

Prior to these three data sets, there were two Styrofoam blocks along the sides of the evaporator, as shown in Figure A.1, that forced all of the airflow over the heat exchanger area. These blocks were taken out and forgotten, possibly the Summer of '92 when the evaporator was replaced by Admiraal and Rubas. Starting with the Spring '94 data set, the blocks were put back in their original location. As expected, the blocks increased the pressure drop across the evaporator and reduced the airflow rate. As a matter of fact, the nominal flow rate for the Spring '94 data

set (with the blocks reinstalled) was estimated to be 67 cfm with an 87% airsplit fraction, which is 5 cfm lower than the previous data set with out the blocks.

Numerous data points taken at the nominal motor speed yielded repeatable estimates of airflow rate and airsplit fraction values at the nominal fan speed. On the other hand, because of the small number of data points taken at each fan speed in the Spring '94 data set, there was not enough information to estimate the airflow rate and airsplit fraction independently at each fan speed. That was not necessary, however, because the baffle position remained unchanged at 87% for all fan speeds. With a constant 87% airsplit fraction assumption for all fan speeds, airflow rate was found to vary linearly with motor speed, and pass through the origin, as shown in Figure A.2. This result is in accordance to the fan laws and validates a constant 87% airsplit fraction assumption for any airflow rate. The estimated fan law relationship for this test evaporator is

$$\overset{\circ}{V} = 0.0207 \cdot \text{RPM} \tag{A.3}$$

where $\overset{\circ}{V}$ is the airflow rate over the evaporator in cfm, and RPM is the fan speed in rpm.
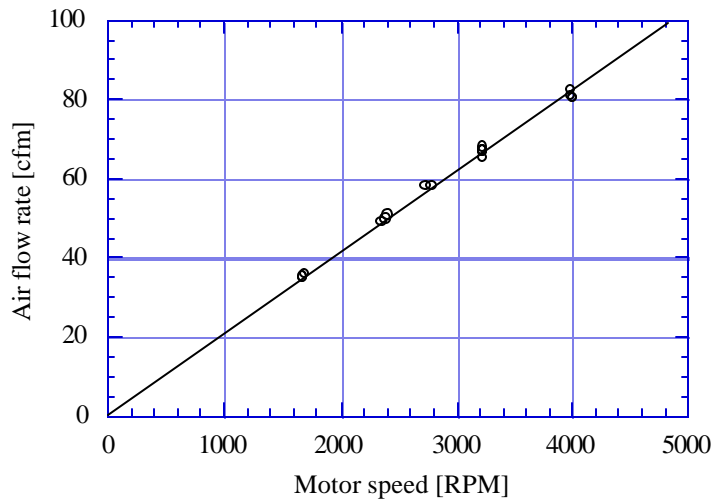
Figure A.2 Fan law relationship

References

Admiraal, D.M., and Bullard, C.W., *Heat Transfer in Refrigerator Condenser and Evaporators*, ACRC TR-48, Air Conditioning and Refrigeration Center, University of Illinois at Urbana-Champaign, 1993.

Appendix B: Evaporator experimental air-side heat transfer coefficients

B.1 Governing equations

Variable-conductance modeling is applied to the two zones of the evaporator shown in Figure B.1. Two separate refrigerant-side heat transfer correlations are used for each zone, while a single air-side heat transfer coefficient is calculated for the whole evaporator.
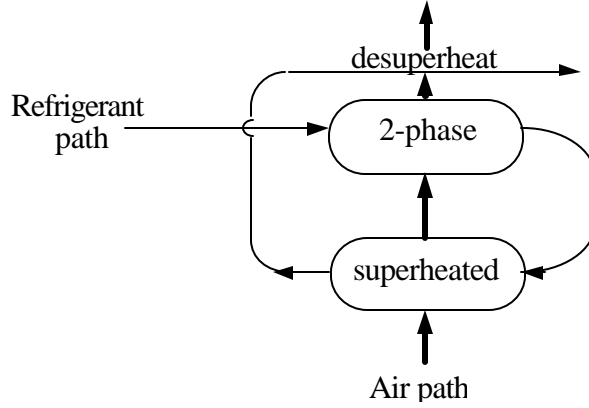
Figure B.1 Evaporator model configuration

Refrigerant-side heat transfer correlation for the two-phase region is the Wattelet et al. (1994) and for the superheated region is the Gnielinsky (Incropera and De Witt, 1990), which are used with the following energy balance equations

$$Q_{tp} = e_{tp} \cdot C_{air} \cdot \left(T_{air,intp} - T_{ref,intp} \right) \tag{B.1}$$

$$Q_{sp} = e_{sp} \cdot C_{ref} \cdot \left(T_{air,insp} - T_{ref,insp} \right) \tag{B.2}$$

$$Q_{dsp} = e_{dsp} \cdot C_{ref} \cdot \left(T_{air,indsp} - T_{ref,indsp} \right) \tag{B.3}$$

$$Q_{sp} + Q_{dsp} = \dot{m}\, \Delta h_{sp,dsp} \tag{B.4}$$

$$Q_{tp} = \dot{m}\Delta h_{tp} \tag{B.5}$$

$$Q_{sp} = C_{air} \left(T_{air,outsp} - T_{air,insp} \right) \tag{B.6}$$

$$Q_{dsp} = C_{air} \left(T_{air,outdsp} - T_{air,outtp} \right) \tag{B.7}$$

$$Q_{tp} = C_{air} \left(T_{air,outtp} - T_{air,outsp} \right) \tag{B.8}$$

$$Q_{cond} = Q_{tp} + Q_{sp} + Q_{dsp} \tag{B.9}$$

where the effectiveness equations for the counterflow geometry are

$$e_{tp} = \left(1 - \exp\left(-\frac{U_{tp}A_{tp}}{C_{air}} \right) \right)$$

(B.10)

$$e_{sp} = \frac{\left(1 - \exp\left(-\frac{U_{sp}A_{sp}}{C_{min,sp}} \cdot \left(1 - \frac{C_{min,sp}}{C_{max,sp}} \right) \right) \right)}{\left(1 - \frac{C_{min,sp}}{C_{max,sp}} \cdot \exp\left(-\frac{U_{sp}A_{sp}}{C_{min,sp}} \cdot \left(1 - \frac{C_{min,sp}}{C_{max,sp}} \right) \right) \right)}$$

(B.11)

$$e_{dsp} = \frac{\left(1 - \exp\left(-\frac{U_{dsp}A_{dsp}}{C_{min,dsp}} \cdot \left(1 - \frac{C_{min,dsp}}{C_{max,dsp}} \right) \right) \right)}{\left(1 - \frac{C_{min,dsp}}{C_{max,dsp}} \cdot \exp\left(-\frac{U_{dsp}A_{dsp}}{C_{min,dsp}} \cdot \left(1 - \frac{C_{min,dsp}}{C_{max,dsp}} \right) \right) \right)}$$

(B.12)

The desuperheating region accounts for having the refrigerant side thermocouple located downstream of a portion of suction line and accumulator which lies in the exit air path, as shown in Figure B.1. In many cases this portion of refrigerant line is recooled by the air that has traveled over the evaporator.

B.2 Parameter estimation

Air-side heat transfer coefficients are determined by energy balance and refrigerant-side heat transfer correlations. The air-side heat transfer coefficient calculated from the Fall '93 data set is compared to Admiraal's Fall '92 and Spring '93 data sets in Table B.1. Results from these three data sets yield the best agreement between the measured and calculated evaporator heat transfer. Admiraal and Bullard (1993) had estimated the inverse of heat transfer coefficient and defined it as a resistance term. In this paper, to eliminate confusion, the heat transfer coefficient is estimated directly, neglecting the resistance of the tube and fin material.

Table B.1 Results of evaporator model at nominal fan speed

	Fall '92	Spring '93	Fall '93
$h_{air} \left[\frac{Btu}{hr\ ft^2\ °F} \right]$	4.83	5.18	4.87

With the Spring '94 data set, the variable-conductance model of the evaporator was tested for different fan speeds and their corresponding range of airflow rates. Most points in this data set were slightly superheated. Both the constant c and the exponent m from Equation 2.22 were estimated by optimizing over the whole data set, as shown in Figure B.2, where each contour represents 10 Btu/hr of the precision interval that ranges from 20 to 210 Btu/hr. Air velocity over the evaporator was estimated by dividing the volumetric airflow rate by the effective cross sectional area of the duct in which the evaporator is located. The effective cross sectional area is $0.323\ ft^2$, which is net of the $0.219\ ft^2$ obstruction due to fins and tubes.
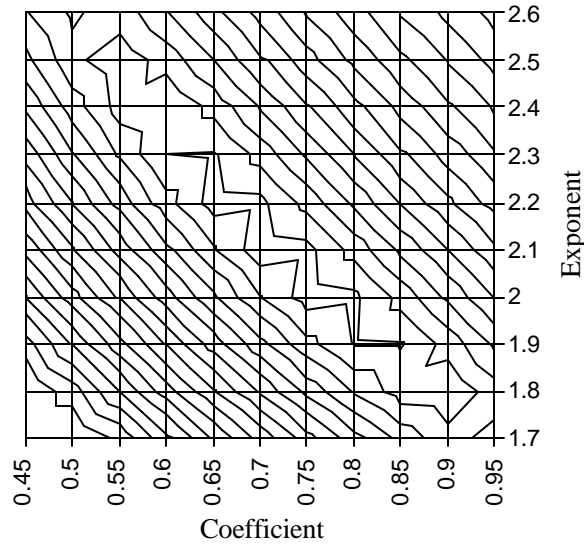
Figure B.2 Precision interval valley

The global minimum has an error of 22 Btu/hr where c = 2.1 and m = 0.72. Numerous combinations of constant c and exponent m give results with errors that are under 40 Btu/hr, which is about 5% of the typical heat capacity of the evaporator. The confidence interval function has a flat and long valley suggesting that the spread of this data set is not large enough to estimate accurately the values of c and m. A wider range of flow rates would be needed to obtain enough information to estimate both parameters with more accuracy.

The experimentally estimated heat transfer coefficients for Spring '94 data set are shown in Figure B.3. At the nominal fan speed, the experimental heat transfer coefficient for the Spring '94 data set is found to be 4.73 $\frac{Btu}{hr\,°F\,ft^2}$, which is 3% lower than for the Fall '93 data set.
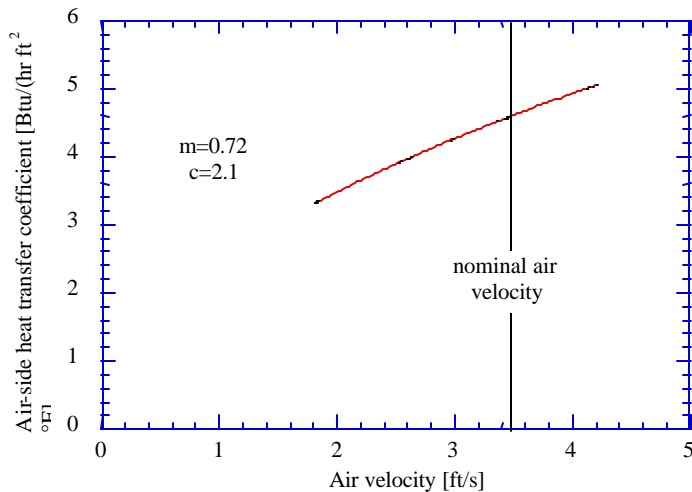
Figure B.3 Air-side heat transfer coefficient for variable flow rates

In Figure B.4, the predicted evaporator load has a 3% confidence interval. The range of loads is between 700 and 800 Btu/hr; airflow rate between 35 and 83 cfm; and evaporator inlet air temperatures between -5 and 15°F.
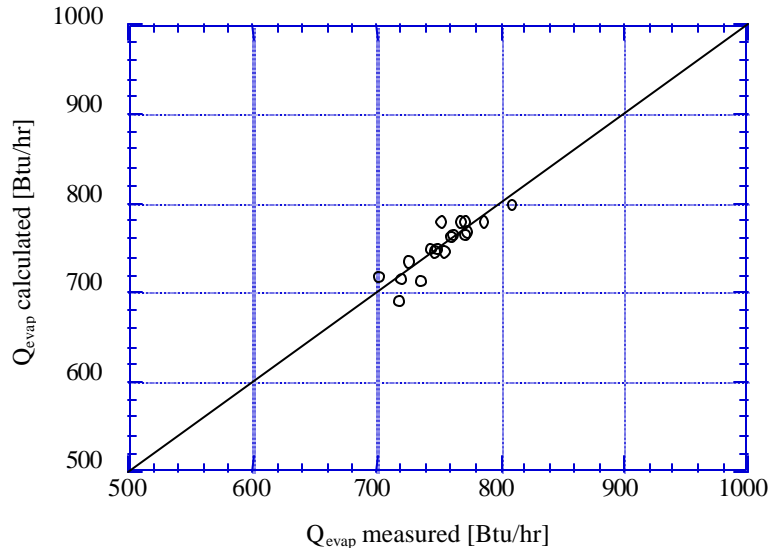
Figure B.4 Measured and calculated evaporator loads

B.3 Effect of superheat on estimating air-side heat transfer coefficient

For the Fall '93 data set, an additional approach was taken for calculating air-side heat transfer coefficient. Values of heat transfer coefficients corresponding to the evaporator heat transfer measured for each data point were computed independently, rather than seeking a single "best" value for the whole data set. For many of the points with superheat above 20°F the estimated air-side heat transfer coefficients had a dual solution (including a solution half that of the actual value), while other points had no solution. This confirms the concerns of Admiraal and Bullard (1993) stating "High amounts of superheat exacerbate the effect of crude geometric approximations". The Fall '92 and Spring '93 data sets display the same type of behavior as the Fall '93 data set. Admiraal and Bullard (1993) found a better confidence interval for their Spring '93 data set than for the Fall '92, because the Spring '93 data set has less data with large superheat.

The relationship between degrees of superheat and superheated area is shown in Figure B.5 for the nominal airflow rate, in the Fall '93 data set. The degrees of superheat are measured, while the superheated area is calculated with the evaporator model. A superheat of 20°F corresponds to 20% of superheat area fraction. At higher levels the geometric approximations are much less accurate and the relationship is nonlinear.
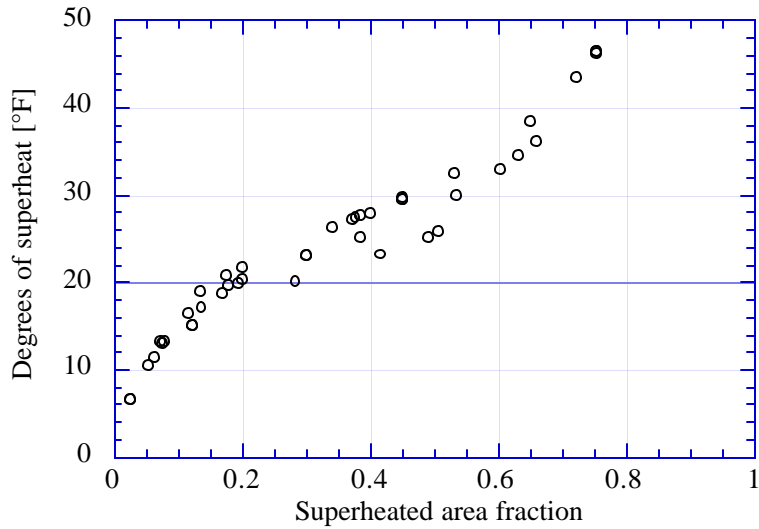
Figure B.5 Superheated area and temperature

For future research, the air-side heat transfer coefficient might be estimated more accurately by using only two-phase evaporator outlet data, which would eliminate any error due to superheat. Also, for other test refrigerators, another refrigerant-side thermocouple could be placed right at the outlet of the evaporator to complement the one downstream of the accumulator and a portion of suction line.

References

Admiraal, D.M., and Bullard, C.W., *Heat Transfer in Refrigerator Condenser and Evaporators*, ACRC TR-48, Air Conditioning and Refrigeration Center, University of Illinois at Urbana-Champaign, 1993.

Icropera, F. P., and De Witt, D. P., *Fundamentals of Heat and Mass Transfer*, 3rd ed., John Wiley & Sons, Inc., New York, 1990.

Wattelet, J.P., Chato, J. C., et al., *Heat Transfer Flow Regimes of Refrigerants in a Horizontal-Tube Evaporator* ACRC TR-55, Air Conditioning and Refrigeration Center, University of Illinois at Urbana-Champaign, 1994.

Appendix C: Condenser calorimeter approach and airflow rate estimation

C.1 Purpose

Air-side heat transfer coefficient calculations require accurate air velocity and airflow rate measurements. An energy balance method is used to determine airflow rate. Unfortunately, flow complexities were found to be a significant source of error by Reeves and Bullard (1992), and Admiraal and Bullard (1993) because of multiple inlets, outlets, and recirculation paths in the test unit. This Appendix describes ways to simplify the configuration of the condenser shown in Figure C.1 and to improve the accuracy of determining flow rate with what is defined the calorimeter setup.
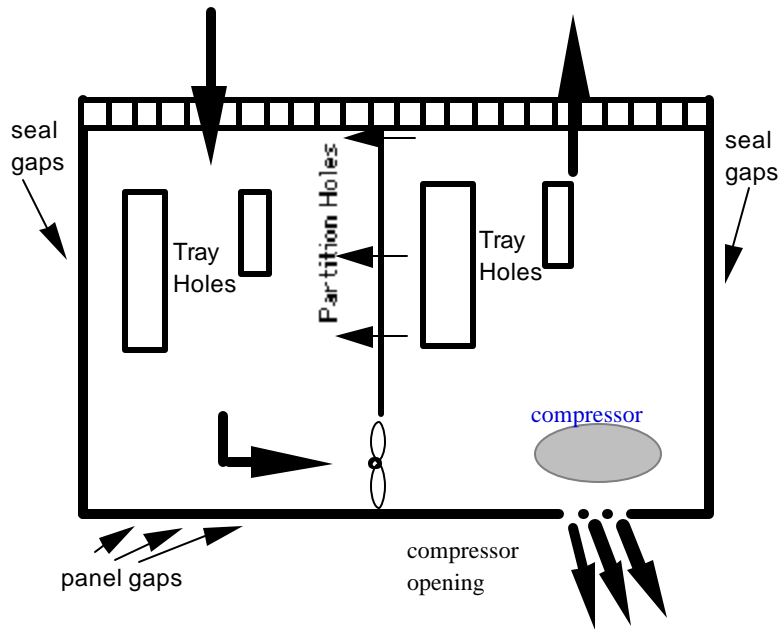
Figure C.1 Condenser Cabinet Geometry

C.2 Background

Reeves and Bullard (1992) calculated a nominal airflow rate over the condenser of the Amana refrigerator which has then been used in the ACRC2 computer model. A flow rate of 106 cfm upstream of the fan was determined using a heater approach, then a 0.35 air fraction exiting behind the compressor was estimated by using measured inlet and outlet temperatures from the operating data set.

Admiraal and Bullard's (1993) calculations were done on the Fall'92 and Spring'93 data sets using a two dimensional optimization. Since there was not enough information to calculate the two parameters accurately, Admiraal used the independently-determined total airflow rate of 110 cfm, and fraction of air exiting behind the compressor of 0.3.

The manufacturer's estimate of the air side flow rate at the fan is 125-150 cfm which is much larger then the results obtained from both Reeves and Admiraal.

C.3 Condenser cabinet configuration

As shown in Figure C.1, the condenser cabinet has a complicated geometry and airflow pattern. Among all complexities, the largest portion of error is most likely caused by the numerous openings in the cabinet that cannot be modeled. Punched out metal tray openings that support the condenser make up approximately 20% of the surface area of the tray and allow air to circulate. The amount of air circulating through the back panel gaps is significant and has varied each time that the back panel was open during instrumentation. Seal gaps between the tray and refrigerator cabinet also allow air infiltration. Even if not easily visible from the outside, partition holes allow air from the downstream region which is in a higher pressure zone to circulate back to the upstream region. This air uses fan capacity, but is not a net benefit to the system.

A 33% internal recirculation is estimated from the temperature profile at the inlet of the condenser described by Admiraal and Bullard (1993). A 30 cfm airflow rate exiting behind the compressor is suggested by Admiraal and Bullard (1993). A 135 cfm airflow rate at the fan is suggested by the manufacturer. From a single data point taken with a heater upstream of the fan, 40 cfm were estimated to enter through the pan, and 65 cfm to enter through the front grille. These two airflow rates add to 105 cfm, which compares well with Reeve's 106 cfm estimate (1992). From the same data point, 25 cfm of the 65 cfm entering the grille are estimated to have recirculate from the grille outlet to the grille inlet. This result compares well with the 30% estimate of Admiraal and Bullard (1993). From a temperature measurement taken when a heater was located downstream of the fan, it was possible to estimate that 60 cfm exited from the grille. By applying conservation of mass to the downstream region of the cabinet, 15 cfm are expected to exit from the pan downstream of the fan.

Other factors responsible for air side complexities are velocity and temperature gradients. Hand held thermocouple measurements show the presence of a large radial temperature gradient right downstream of the fan as shown in Figure C.2. An electrical heater delivering 300 Watts evenly distributed across the condenser cabinet entrance causes a gradient of 6.5° F just downstream of the fan. During normal refrigerator operation even larger gradients have been measured.
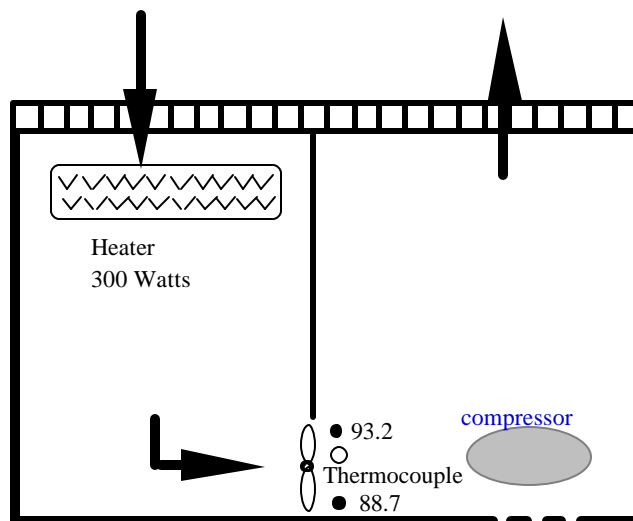
Figure C.2 Temperature measurement just downstream of the fan

In all data sets previous to July 29, 1993 the thermocouple just downstream of the fan was not mounted well and was lying on the bottom of the pan. Since this temperature reading agreed with the one of the air leaving behind the compressor, it was thought that there was perfect air mixing just downstream of the fan and that the thermocouple measurement was accurate. Measured gradients with the heater setup and during refrigerator operation indicate that the air does not mix well just downstream of the fan and that this measurement is not accurate enough to be used for energy balance calculations.

Hand-held thermocouple measurements showed the presence of gradients at the inlet and outlet of the condenser cabinet. During refrigerator operation the outlet temperature gradient has a standard deviation up to 2.0°F for conditions with large desuperheating, which is eliminated by using the heater setup shown in Figure C.2. Inlet grille temperature gradients, which are caused by the recirculation of warmer air from the outlet, are eliminated as well. Since all of these temperature gradients cannot be modeled, they should be eliminated or at least reduced.

C.4 Calorimeter geometry

Condenser airflow rate estimates of Admiraal and Bullard (1993) and Reeves and Bullard (1992) had many uncertainties due to numerous air-side complexities. Since the purpose of the variable conductance model is not to model all of these complexities, but to determine accurately air-side heat transfer coefficients and performance of the test refrigerator at different airflow rates, the calorimeter approach, which gives better air-side measurements and makes the modeling of the condenser cabinet much easier, was used.

This calorimeter set up involves modifying the condenser cabinet in such matter that all of the openings other then grill inlet and outlet are sealed with duct tape. Therefore seal gaps, tray holes, partition holes, back panel gaps, and opening behind the compressor are all closed off. Sealing all of these openings will increase the pressure drop across the condenser and possibly affect the airflow rate, which would be specific to a particular configuration.

Thermocouples at the inlet and the outlet of the condenser cabinet are placed in an array which is kept in place by the cardboard frame shown in Figure C.3. A partition is placed between the inlet and outlet airstream to fend off recirculation and reduce the temperature gradient of the inlet air as much as possible. As a matter of fact, with the partition the airstream inlet gradient is only 0.4°F regardless of the amount of superheat of the condenser.

The thermocouple array spans horizontally neglecting possible temperature gradients in the vertical direction. Each inlet thermocouple is equally distant from each other and covers approximately the same airstream cross sectional area. Outlet thermocouples 6 through 10 also cover the same airstream cross sectional area, while outlet thermocouples 5 and 11 are placed at the extreme horizontal locations to monitor the full range of air temperatures.

While the inlet thermocouples are averaged with a thermopile which physically averages the temperatures by connecting them in parallel, each outlet thermocouple is recorded and averaged algebraically. Since the partition eliminates temperature gradients at the inlet, it is not necessary to record each thermocouple separately at the inlet. Similarly, monitoring the airstream temperature gradient at the outlet, will give insight on the uncertainties in estimating airflow rate.
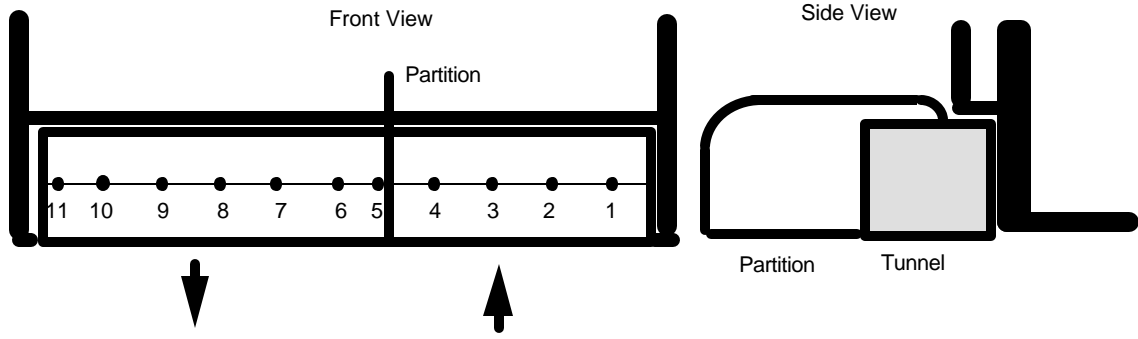
Figure C.3 Thermocouple Layout at Inlet and Outlet of Condenser Cabinet

C.5 Airflow rate estimation

Airflow rate over the condenser is calculated with the calorimeter setup. This type of setup is simple, eliminates the need of estimating fractions of air exiting behind the compressor, and gives accurate results. An additional modification to the condenser is the removal of the front grille to achieve higher airflow rates. Airflow rate measurements are done by drawing an energy balance around the condenser cabinet and by solving the equation

$$C_{air} (T_{air,out} - T_{air,in}) = Q_{load} \qquad (C.1)$$

where C_{air} is the heat capacity of the air, $T_{air,out}$ and $T_{air,in}$ are outlet and inlet air temperatures, and Q_{load} is the heat transfer to the condenser cabinet.

Heat can be delivered to the condenser cabinet by operating the refrigerator during steady state conditions:

$$C_{air} (T_{air,out} - T_{air,in}) = Pwr_{cond} + Pwr_{comp} + \dot{m}_{ref} (h_{ref,outsb} - h_{suc}) \qquad (C.2)$$

where $\dot{m}_{ref}$ is the mass flow rate of the refrigerant, $h_{ref,outsb}$ and h_{suc} are the enthalpy of the refrigerant entering and exiting the condenser cabinet, and Pwr_{cond} and Pwr_{comp} are the power reading of the condenser fan and of the compressor.

A different way of delivering heat to the condenser cabinet is with an electrical heater:

$$C_{air} (T_{air,out} - T_{air,in}) = Pwr_{cond} + Pwr_{heater} \qquad (C.3)$$

where Pwr_{heater} is the power delivered by the heater. The heater is placed in the upstream region of the condenser cabinet and the power is delivered uniformly across the inlet airflow.

When the refrigerator is operating the outlet air temperature has a significant temperature gradient, while with the heater setup the temperature is uniform. Since the heater setup gives more accurate temperature readings at the outlet it is used in calculating airflow rate as a function of motor speed.

C.6 Varying motor speed and airflow rate

The controller has the capability of varying the speed of the motor from 200 to 2250 revolutions per minute. While the controller ability to deliver power is the limiting factor to reach higher motor speeds and airflow rates, the need of subcooled points at the outlet of the condenser defines the lower limit. During the experimental procedure, surface thermocouples located in regions of the condenser which are always two-phase, monitor the condensing temperature and the amount of subcooling at the condenser exit temperature.

The fan laws in ASHRAE Equipment Handbook (1972) state that the airflow rate is directly proportional to the fan speed, everything else being equal. In Figure C.1, the volumetric airflow rate is calculated both from operating conditions of the test refrigerator and from the heater setup. Three different operating conditions, which are set by controlling the temperature of the fresh food and freezer compartments and consequently the load to the evaporator, are tested and compared to the heater setup. The operating conditions with the largest desuperheating deviate the most from the heater results, especially at the higher flow rates. Higher velocities and desuperheating conditions introduce velocity and temperature gradients which are a source of error in calculating airflow rate.
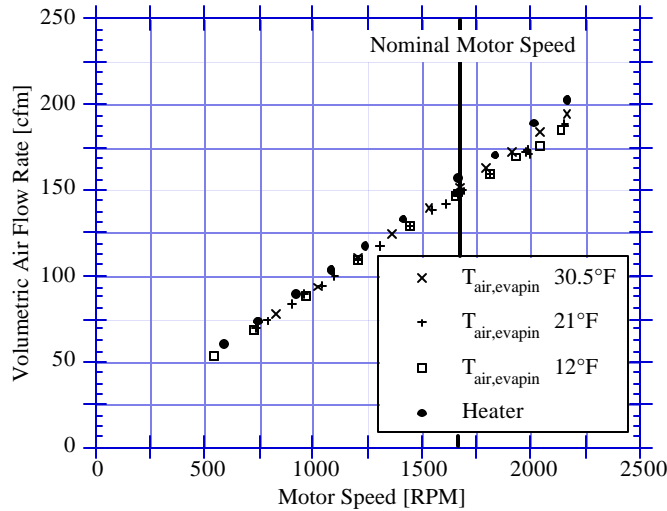
Figure C.1 Calculating flow rate with heater or refrigerator load

The equation for flow rate as a function of motor speed is estimated using the heater results. As expected the results are linear:

$$\overset{\circ}{V}_{air} = 3.99 + 0.0912 \, \text{RPM} \tag{C.4}$$

where $\overset{\circ}{V}_{air}$ is the airflow rate and RPM is the motor speed. This equation can only be used with this particular configuration. As a matter of fact, at the nominal fan speed airflow rate is 158 cfm without the grille, but 120 cfm with the grille on. For both Fall '93 and Spring '94 data sets the grille was removed in order to obtain data over the widest range of velocities. It is evident that variations in geometric configuration affect the pressure drop across the fan and consequently the airflow rate. It is unfortunate that the are no air-side pressure drop measurements across the condenser to relate pressure drop and airflow rate.

References

Admiraal, D.M., and Bullard, C.W., *Heat Transfer in Refrigerator Condenser and Evaporators*, ACRC TR-48, Air Conditioning and Refrigeration Center, University of Illinois at Urbana-Champaign, 1993.

ASHRAE, *Equipment*, Guide and Data Book, 1972.

Reeves, R.N., Bullard, C.W., and Crawford, R.R., *Modeling and Experimental Parameter Estimation of a Refrigerator/Freezer System*, ACRC TR-9, Air Conditioning and Refrigeration Center, University of Illinois at Urbana-Champaign, 1992.

Appendix D: Condenser experimental air-side heat transfer coefficient

D.1 Governing equations

Variable conductance modeling is applied to the calorimeter setup described in Appendix C. Refrigerant-side correlations listed in Chapter 2 and first law principle are used to estimate air-side heat transfer coefficients for different fan speeds. The condenser is divided into a total of four different regions: a superheated, a two-phase downstream of the fan, a two-phase upstream of the fan and a subcooled, as shown in Figure D.1. Four different refrigerant-side heat transfer coefficients are required for each zone, while two separate air-side heat transfer coefficients are needed for the upstream and downstream regions of the condenser to account for the different air velocities between the two. Air velocity is larger in the upstream region due to the smaller cabinet cross sectional area and higher wire and tube obstructions
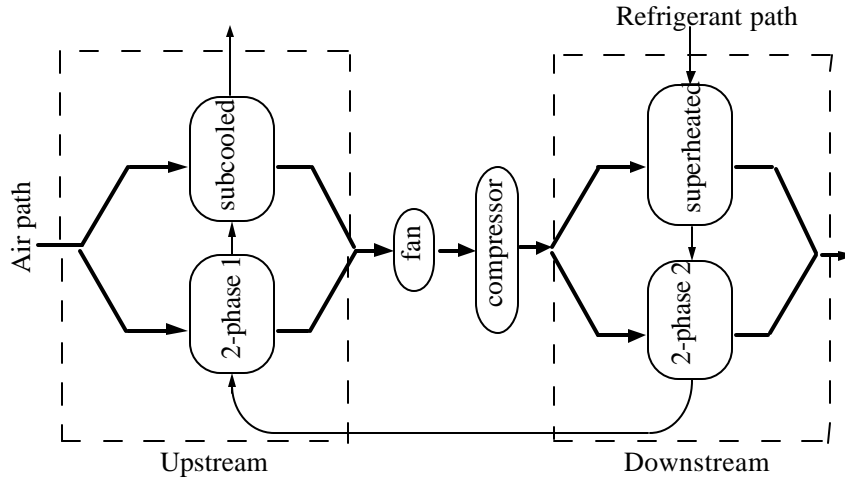
Figure D.1 Condenser model configuration

The refrigerant-side heat transfer correlation used for the two-phase region is the Chato/Dobson (Admiraal and Bullard, 1993), while for the superheated and subcooled regions is the Gnielinsky (Admiraal and Bullard, 1993). The form of air-side heat transfer correlation used is Equation 2.15. Energy balance of the condenser is defined by the equations

$$Q_{sb} = e_{sb} C_{ref,sb} \left(T_{ref,2} - T_{air,incond} \right) \tag{D.1}$$

$$Q_{tp1} = e_{tpl} C_{air,tp1} \left(T_{ref,2} - T_{air,incond} \right) \tag{D.2}$$

$$Q_{tp2} = e_{tp2} C_{air,tp2} \left(T_{ref,2} - T_{air,mid} \right) \tag{D.3}$$

$$Q_{sp} = e_{sp} C_{ref,sp} \left(T_{ref,1} - T_{air,mid} \right) \tag{D.4}$$

$$Q_{sb} + Q_{tp1} + Pwr_{fan} + Q_{comp} = C_{air,sb} \left(T_{air,mid} - T_{air,incond} \right) \tag{D.5}$$

$$Q_{sp} + Q_{tp2} = C_{air} \left(T_{air,outcond} - T_{air,mid} \right) \tag{D.6}$$

$$Q_{sb} = \dot{m}^2 ? h_{sb} \tag{D.7}$$

$$Q_{tp} = \dot{m}^2 ? h_{tp} \tag{D.8}$$

$$Q_{sp} = \dot{m}^2 ? h_{sp} \tag{D.9}$$

$$Q_{tp} = Q_{tp1} + Q_{tp2} \tag{D.10}$$

$$Q_{cond} = Q_{sb} + Q_{tp} + Q_{sp} \tag{D.11}$$

where the effectiveness equations for this parallel-counterflow geometry are

$$e_{sb} = \frac{2}{\sqrt{1 + \left[\dfrac{C_{ref,sb}}{C_{air,sb}}\right]^2}\left(\dfrac{1 + e^{-\Gamma_{sb}}}{1 - e^{-\Gamma_{sb}}}\right) + \left[1 + \dfrac{C_{ref,sb}}{C_{air,sb}}\right]} \tag{D.12}$$

$$e_{sp} = \frac{2}{\sqrt{1 + \left[\dfrac{C_{ref,sp}}{C_{air,sp}}\right]^2}\left(\dfrac{1 + e^{-\Gamma_{sp}}}{1 - e^{-\Gamma_{sp}}}\right) + \left[1 + \dfrac{C_{ref,sp}}{C_{air,sp}}\right]} \tag{D.13}$$

$$e_{tp1} = 1 - \exp\left[\frac{-U_{tp}A_{tp1}}{C_{air,tp1}}\right] \tag{D.14}$$

$$e_{tp2} = 1 - \exp\left[\frac{-U_{tp}A_{tp2}}{C_{air,tp2}}\right] \tag{D.15}$$

and

$$\Gamma_{sb} = \frac{U_{sb}A_{sb}}{C_{ref,sb}}\sqrt{1 + \left[\frac{C_{ref,sb}}{C_{air,sb}}\right]^2} \tag{D.16}$$

$$\Gamma_{sp} = \frac{U_{sp}A_{sp}}{C_{ref,sp}}\sqrt{1 + \left[\frac{C_{ref,sp}}{C_{air,sp}}\right]^2} \tag{D.17}$$

Each region has its own air-side heat capacity which is proportional to the surface area. As the surface area of each region increases, a larger portion of the air travels over it and consequently the heat capacity increases as well. Compressor and fan heat transfer are included in the model by assuming perfect mixing and sequential air path over the compressor and then over the downstream region.

D.2 Variable air side heat transfer coefficients

In Figure D.2, each air-side heat transfer coefficient is estimated at different airflow rates for the upstream and downstream regions of the condenser.
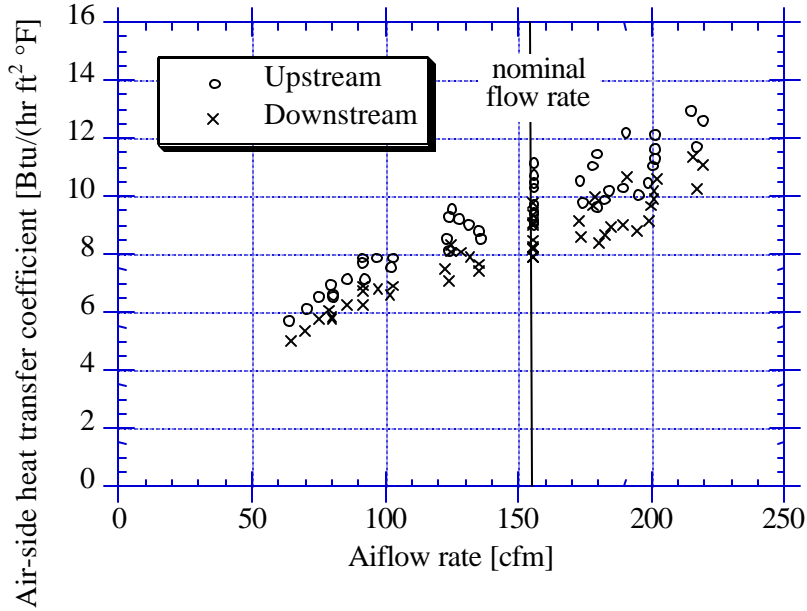
Figure D.2 Inverse of air side conductance versus flow rate

As expected, the air-side heat transfer coefficient is larger at higher volumetric flow rates and in the upstream region of the condenser, which has a narrower cabinet cross sectional area. Higher velocities can be achieved by increasing flow rate or with smaller condenser cabinet cross sectional areas, but, in both cases, at the expenses of higher fan power requirements.

Although it is common to talk in terms of volumetric airflow rate, it makes more sense to describe air-side conductance in terms of air velocity, as shown in Figure D.3. Air velocity is calculated by dividing the volumetric airflow rate by the effective airstream cross sectional area. The upstream region has a cross sectional area of $0.400 \, \text{ft}^2$, which includes a $0.031 \, \text{ft}^2$ obstruction of fin and tubes, while the downstream region has a cross sectional area of $0.525 \, \text{ft}^2$, which includes a $0.013 \, \text{ft}^2$ obstruction of fin and tubes. As expected, the air-side heat transfer coefficients for the upstream and the downstream regions overlap each other when plotted against velocity since they have the same characteristic geometry. An exponent m equal to 0.53 and constant c equal to 3.51 from Equation 2.22 are estimated by curve fitting the best agreement of air-side heat transfer coefficients shown in Figure D.3.

29

Figure D.3 Air-side heat transfer coefficient versus velocity

The different layout between the upstream region, which has three layers of wires and tubes, and the downstream region, which has only one, does not seem to affect the results even at lower velocities when the boundary layer is larger. Simple theoretical calculations show that the boundary layer thickness for a flat plate with the same scale length and with a low air velocity of 2 ft/s is 0.7 inches. The boundary layer should be larger than 1.2 inches, which is half of the spacing between co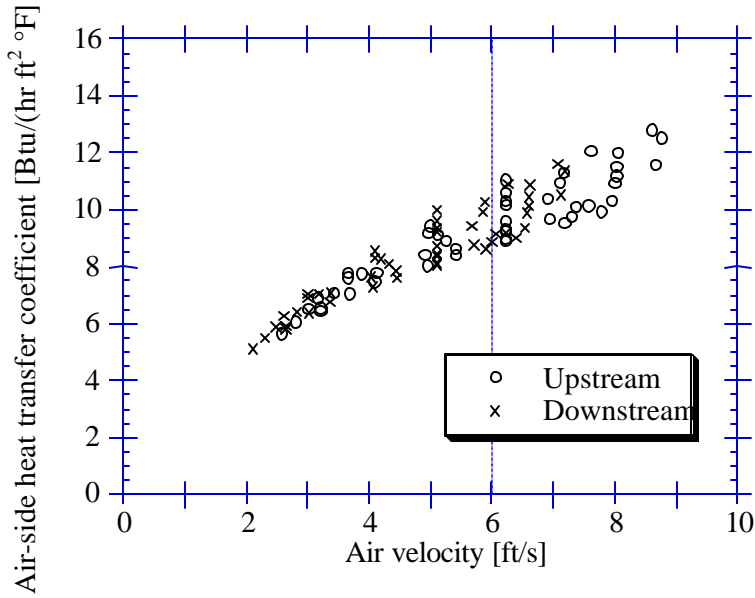ndenser layers, to have any effect on air-side heat transfer. If the layer were larger than 1.2 inches, the air-side heat transfer correlation should include a condenser layout dependence.

Air-side heat transfer coefficients at the nominal fan speed are $9.09 \dfrac{\mathrm{Btu}}{\mathrm{hr\,ft}^2\,^\circ\mathrm{F}}$ for the upstream region and

$8.20 \dfrac{\mathrm{Btu}}{\mathrm{hr\,ft}^2\,^\circ\mathrm{F}}$ for the downstream region. These values are both lower than the single heat transfer coefficient 9.8

$\dfrac{\mathrm{Btu}}{\mathrm{hr\,ft}^2\,^\circ\mathrm{F}}$ estimated by Admiraal and Bullard (1993) for both regions. Admiraal and Bullard (1993) did not have the calorimeter setup, which is most likely responsible for the discrepancy.

According to Coulter (1994), there was a refrigerant leak during the Fall '93 data set: the test started with a charge of 11.6 oz, but finished up a month later with only 8.6 oz. Once the leak was fixed, the Spring '94 data set had a charge of 8.0 oz with no leaks (Coulter, 1994).

D.3 Factors contributing to uncertainty

The attempt to determine the cause of the scatter for the air-side heat coefficient results involves determining possible trends. Several are the possible sources of error to be considered. In Figure D.4, eight well defined curves for each of the operating conditions have exponents between 0.49 and 0.56 and seem to depend on the load of the evaporator. As a matter of fact, for higher airstream inlet temperatures to the evaporator or for higher chamber temperatures, the air-side heat transfer coefficients seem to be higher.

Air-side heat transfer coefficient [Btu/(hr ft^2 °F)]

Air velocity [ft/s]

	Evaporator inlet air T [°F]	Chamber T [°F]
○	12	58
□	21	58
◇	31	58
×	12	75
+	21	75
△	31	75
●	21	88
■	31	88
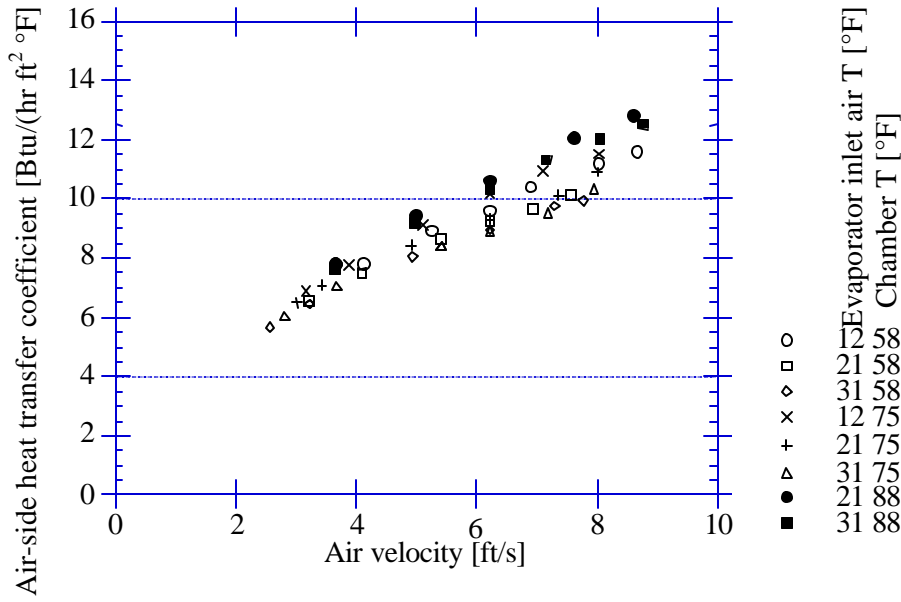
Figure D.4 Upstream heat transfer coefficient for the different operating conditions

D.3.1 Natural convection

The fact that higher chamber temperatures seem to have larger air-side heat transfer coefficients would give the impression that buoyant forces are not negligible. Contrarily, since scatter of the estimated air-side heat coefficients is larger at the higher airflow rates, it eliminates the possibility of error due to neglecting natural convection, which, contrarily, should affect the lower airflow rates, where forced convection is lower..

D.3.2 Heat transfer through cabinet walls

Heat losses through the uninsulated condenser cabinet side-walls were determined not to be the source of the scatter. This phenomenon is difficult to model with accurate correlations since the heat transfer coefficient of the condenser cabinet walls is unknown. A sensitivity analysis for the wall conductance of the refrigerator/freezer compartment showed that different amounts of heat loss through the walls does not affect the scatter, but only the bias.

D.3.3 Refrigerant mass flow rate

A sensitivity analysis showed that bias in refrigerant-side mass flow rate measurements increases or decreases the heat transfer coefficients without affecting the scatter.

D.3.4 Refrigerant-side correlations

Another possible source of error is the refrigerant side empirical heat transfer correlation for single phase flow. If this were true, the largest amount of error should occur when the largest amount of subcooling or superheat is present.
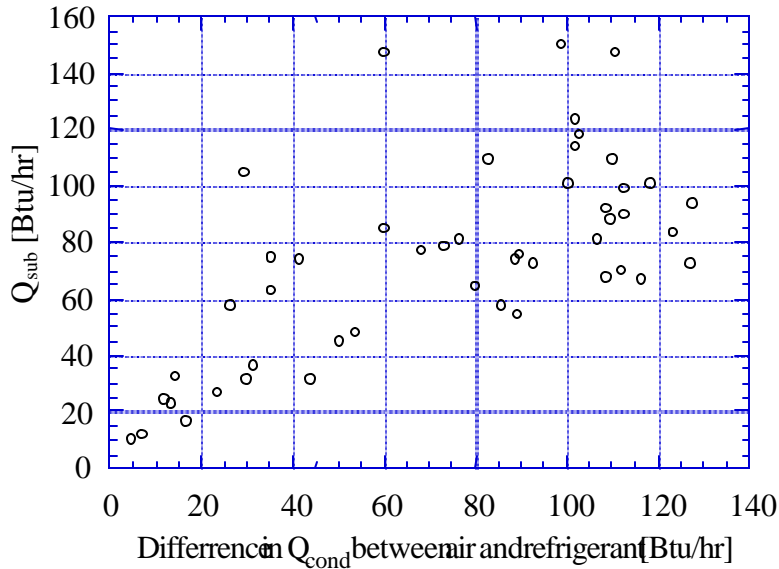
Figure D.5 Difference between air and refrigerant-side condenser load calculations

As shown in Figure D.5, as subcooling increases the discrepancy in calculated condenser load between the air-side and the refrigerant-side increases as well. Since there is no other way of testing the accuracy of the refrigerant-side correlations developed by Admiraal and Bullard (1993), this could indicate that they could be in part responsible of the variation in air-side heat transfer coefficient results. There is not a similar trend in the superheated region, which would support the idea that the Gnielinski correlation is inaccurate in the subcooled region of the condenser, but works well for the desuperheating region.

D.3.5 Radiative losses

Radiative heat transfer could be significant for the measured temperature differences between the surroundings and the condenser. A separate project under Professor Clausing will investigate this problem. A brief sensitivity analysis shows that operating conditions with larger radiative heat transfer potential are not associated with points with the larger difference between air and refrigerant-side condenser load.

References

Admiraal, D.M., and Bullard, C.W., *Heat Transfer in Refrigerator Condenser and Evaporators*, ACRC TR-48, Air
    Conditioning and Refrigeration Center, University of Illinois at Urbana-Champaign, 1993.

Appendix E: Refrigerant mass flow rate and compressor input power

E.1 Refrigerant mass flow rate

Refrigerant-side mass flow rate is an important measurement used in energy balance and refrigerant-side heat transfer coefficient correlations. It has been noticed that even small variance in mass flow rate can have large effects in estimating subcooling and superheating (Admiraal and Bullard, 1993).

There are three methods of determining mass flow rate in our test refrigerator. The first one is with a Sponsler liquid mass flow meter, which is located at the outlet of the condenser. This device works only when the refrigerant is subcooled. The mass flow meter had been originally calibrated with a Micromotion coriolis-type flow meter (Admiraal and Bullard, 1993). Since then it has clogged several times and has been removed and cleaned with out being recalibrated. The clogging and cleaning processes could have effected the calibration.

The second method of calculating mass flow rate is with the compressor map, which is a biquadratic curve fit of the compressor inlet and outlet saturation temperatures.

The last method of calculating the mass flow rate involves the energy balance of the evaporator:

$$Q_{evapload} = \overset{?}{m}_{ref}\ \Delta h_{evap} \tag{E.1}$$

where Δh_{evap} is the change in enthalpy of the refrigerant line across the evaporator, and $Q_{evapload}$ is the load delivered to the evaporator by cabinet heat gain and by the heaters. Possible errors could be caused by assuming that cabinet conductance is independent of ambient and chamber temperatures, and by uncertainties in temperature and power measurements.

These flow rates measurements are shown in Figure E.1 for the Fall '93 data set. Each method follows the same trend, but with a bias. Flow meter measurements underestimate mass flow rates up to 20% from the energy balance approach. Admiraal and Bullard (1993) had previously noticed that the flow meter underestimated flow rate only up to 8% from the energy balance. Between these two data sets the meter was disassembled and cleaned once, which evidently affected its calibration. The compressor map overestimates the flow rate up to 5% relative to the energy balance method for the Fall '93 data set which is similar to the results obtained from Admiraal and Bullard (1993) in the Spring '93 data set.
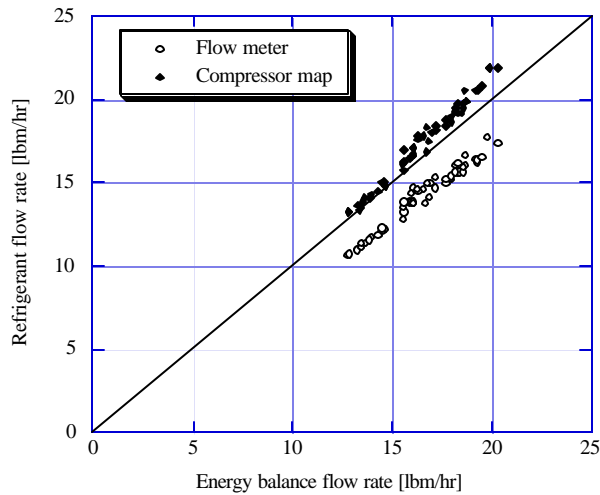
Figure E.1 Mass flow rate measurements for Fall '93 data set

Possible errors due to temperature dependence of the foam conductivity must also be addressed to trust the energy balance method. The variable conductance of the foam as a function of temperature is calculated assuming a typical slope of $0.01 \dfrac{\text{BTU in}}{\text{hr ft}^2 \ \text{°F}}$ and is applied to the average temperature of the freezer and fresh food compartment at each ambient temperature. The difference between assuming a constant or variable cabinet foam conductance affects all results less than 1%.

Generic compressor maps supplied by manufacturers are generally accurate within only 5%. Figure E.1 shows that the map is 5% off from the energy balance measurement, which might not seem to be a large offset, but which is a significant error when the mass flow rate map is used to calculate condensing temperature at a given evaporating temperature and mass flow rate, as done in compressor model of Appendix F. Since large changes in condensing temperature have only a small effect on mass flow rate, small errors in modeling mass flow rate affect significantly the modeled condensing temperature. For example, if map and measured flow rates disagree by 5%, it will produce errors of 28°F in condensing temperature and 80 psi in condensing pressure. For another compressor this might not be the case; the Tecumseh 1390 compressor in the test refrigerator had a mass flow rate that was quite insensitive to changes in condensing pressure and temperature.

E.2 Compressor power

Input power to the compressor is calculated in two different ways. The first way is with a power transducer and the second one is with a compressor map. For the input power transducer, the manufacturer's estimated error is ±7.5 Watts. As shown in figure E.2, the two different methods of measuring power agree with one another.
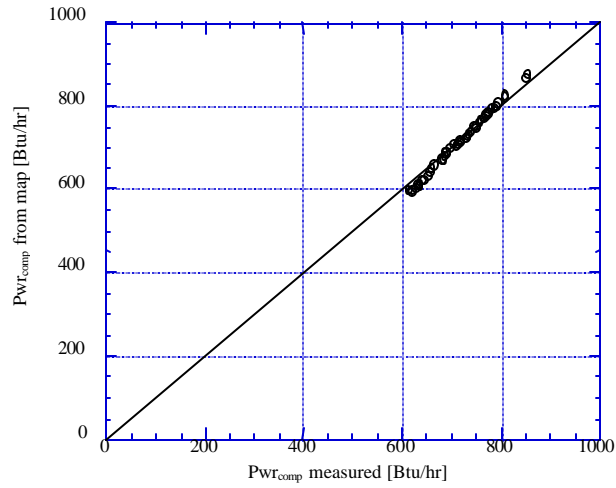
Figure E.2 Power measurements for Fall '93 data set

References

Admiraal, D.M., and Bullard, C.W., *Heat Transfer in Refrigerator Condenser and Evaporators*, ACRC TR-48, Air Conditioning and Refrigeration Center, University of Illinois at Urbana-Champaign, 1993.

Appendix F: Compressor heat transfer coefficients

F.1 Governing equations

The first-law energy balance of the compressor relates input power, convective heat transfer from the shell, and enthalpy change in the refrigerant across the compressor:

$$Pwr_{comp} = \dot{m}_{ref} \cdot \Delta h_{ref} + Q_{comp} \qquad \text{(F.1)}$$

where Δh_{ref} is the change in refrigerant enthalpy across the compressor, $\dot{m}_{ref}$ is the refrigerant mass flow rate, Pwr_{comp} is the power input, and Q_{comp} is the heat transfer of the compressor, which can be defined in terms of the convection heat transfer equation, known as Newton's law of cooling:

$$Q_{comp} = h_{air,comp} \cdot A_{comp} \cdot (T_{dome} - T_{air}) \qquad \text{(F.2)}$$

where $h_{air,comp}$ is the heat transfer coefficient, A_{comp} is the surface area of the compressor exposed to the airstream (1.2 ft^2), T_{dome} is the dome temperature and T_{air} is the temperature of the air downstream of the fan. The dome temperature had been chosen to describe the shell temperature, since it is close to the measured average shell temperature.

F.2 Shell temperature

Air temperature can be measured with a thermocouple located just downstream of the fan or it can be calculated by energy balance of the condenser cabinet upstream of the fan. Since Appendix C showed that the thermocouple measurement is not accurate because of the significant radial temperature gradient in the air downstream of the fan, the air temperature is calculated from the upstream condenser heat transfer. Surface temperature of the compressor is measured at the four locations shown in Figure F.1.

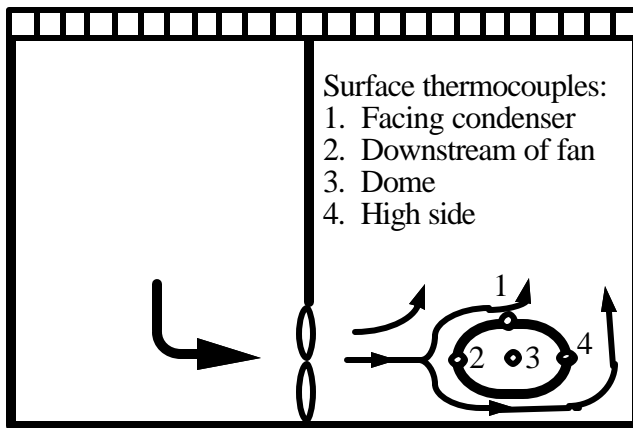Figure F.1 Surface thermocouple location for compressor shell

Shell temperature gradient, as shown in Figure F.2, is representative of uneven cooling, complicated airflow patterns, and compressor geometry characteristics. As expected, the thermocouples on the high side and the top of the shell, which are not directly hit by the airflow and are closer to the refrigerant discharge, measure a higher

temperature than the ones downstream of the fan and facing the condenser, which are directly exposed to the airflow of the fan and are farther away from the refrigerant discharge.

Constant offset among the different shell thermocouples eliminates the possibility of random error, but introduce the possibility of systematic error in determining the average shell temperature. Also, since the data was taken at different airflow rates, the constant offset indicates that there is little air stagnation by the thermocouples not directly exposed to the airflow, and that forced convection is the major mode of heat transfer for the compressor.

The dome temperature is close to the arithmetically calculated average temperature of all four locations, and it will be used as the shell temperature because it is frequently recorded at the rating point condition.
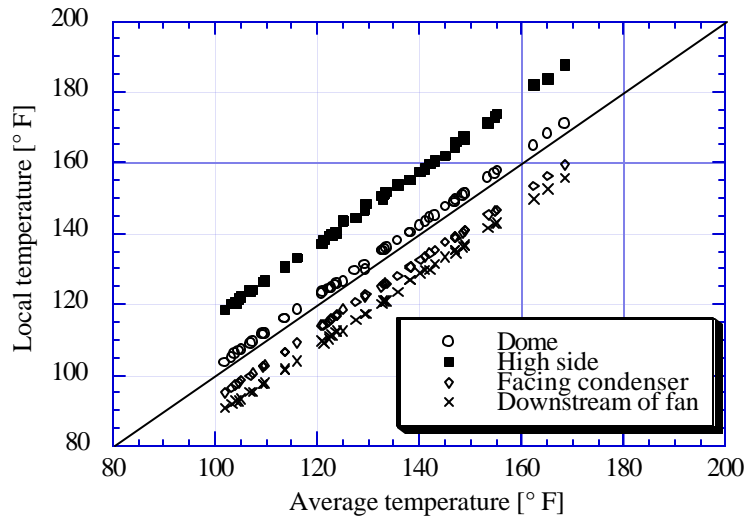

Figure F.2 Measured surface temperature gradient on compressor shell

F.3 Air-side heat transfer coefficients

Air-side correlations for geometries similar to the shape of the compressor are compared to the experimental results at each data point of the Fall '93 data set, as shown in Figure F.3. Flat plate, sphere, and cylinder geometries are considered. Using the average diameter of the compressor can (6 inches) as length scale, Reynolds number ranges between 2×10^4 and 5.1×10^4. Air velocity for the experimental results is determined by dividing the airflow rate by the cross sectional area of the fan, which has a 6 in diameter. Since velocities are directly proportional to one another for different cross sectional areas, assuming the wrong area would change the value of the constant c in Equation 3.1, but since this area is consistently used throughout the paper, it will not affect the prediction of convective heat transfer and outlet conditions.

The theoretical correlation for a flat plate with laminar flow is

$$\mathrm{Nu} = 0.664 \cdot \mathrm{Re_L}^{0.5} \cdot \mathrm{Pr}^{0.36} \qquad\qquad\qquad (F.3)$$

where the characteristic length is equal to half of the circumference of the can. The Whitaker correlation (Incropera and De Witt, 1990) for a sphere is

$$Nu = 2 + (0.4 \cdot Re_D^{0.5} + 0.06 \cdot Re_D^{0.66}) \cdot Pr^{0.33} \cdot \left(\frac{\boldsymbol{m}}{\boldsymbol{m}_s}\right)^{0.25}$$

(F.4)

where the length scale is determined by assuming an average compressor diameter of 6 inches. The Zhukauskas correlation (Incropera, 1990) for a cylinder with $10^3 < Re_D < 2 \times 10^5$ is

$$Nu = 0.26 \cdot Re_D^{0.6} \cdot Pr^{0.37}$$

(F.5)

where the length scale is also determined by assuming an average compressor diameter of 6 inches. Prandtl number varies less than 1% in all of the above correlations for the Fall '93 data set.
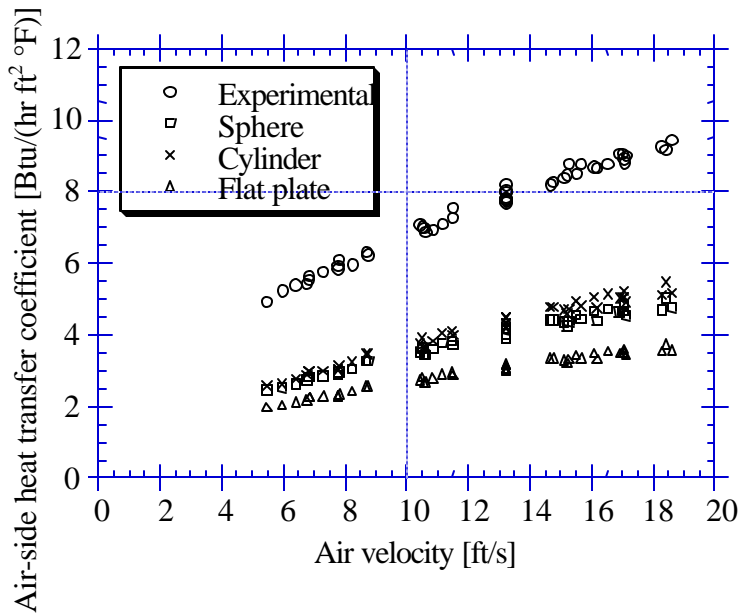

Figure F.3 Experimental and theoretical air-side heat transfer coefficients

A possible explanation for the experimental heat transfer coefficients being two times larger than suggested by the correlations is that the compressor is attached to a floor pan which could act as a fin. To make up for the difference, the surface area would have to include an additional 1.2 ft^2 (the total surface area of the tray is about 4.1 ft^2). Inaccurate shell or air temperatures could also be in small part responsible: an error of 5°F in determining either the air or the shell temperature would affect by 5-12% the estimated air-side heat transfer coefficient.

One way of determining the constant and the exponent of Equation 3.3, is to minimize the mean squared error of the air-side heat transfer coefficients determined for the 48 data points shown in Figure F.3. Another approach is to find the values of the coefficients that produce the best agreement between predicted and calculated compressor heat transfer. Either method gives basically identical answers with similar precision intervals, as shown in the first two rows of Table F.1.

In Table F.1, the confidence interval is fairly sensitive to different combinations of c and m, indicating that there is enough information in the data set to estimate these two parameters. Naturally, a data set spanning a wider range of air velocities would give more accurate results.

As mentioned earlier, theoretical and empirical correlations for cylinders, spheres and flat plates seem to have the exponent m = 0.5 or 0.6. The exponent m = 0.5 is an accepted exponent for a flat plate or a sphere, and gives good results as shown by the confidence interval. To enable the modeler to estimate only one parameter by making use of data given for the rating point of the compressor, the exponent m will be assumed equal to 0.5.

Table F.1 Parameters for heat transfer correlation using the shell temperature

Objective function	c	m	Precision interval of Q_{comp} [Btu/hr]
$h_{air,comp}$	1.987	0.517	20.1
Q_{comp}	1.981	0.518	19.9
Q_{comp} (set m = 0.5)	2.071	0.5	20.8
Q_{comp} (set m = 0.6)	1.617	0.6	32.9
Q_{comp} (set m = 0.4)	2.650	0.4	43.4

F.3 Relating compressor shell and discharge temperatures

While results are satisfying theoretically, the modeler has the problem of developing an equation predicting the surface temperature of the shell as a function of the air and refrigerant-side variables, and of the compressor characteristics. Therefore, the surface temperature is replaced in some simulation models (e.g. ADL, 1982; Merriam et al., 1993) by the discharge temperature, which, unlike the shell temperature, is a variable that already appears in the model's compressor energy balance. In this situation, when the dome temperature is not known or cannot be estimated, the following convective heat transfer equation is used

$$Q_{comp} = h_{air,comp} A_{comp} (T_{dis} - T_{air}) \qquad\qquad (F.6)$$

The correct form of the convective heat transfer equation uses the dome temperature. There is no theoretical basis for using the discharge temperature, and the data show clearly that the discharge and shell temperature differ greatly. Consequently, the estimated air-side heat transfer coefficient using the discharge temperature convection heat transfer equation is a crude approximation and differs from the actual air-side heat transfer coefficient using the dome temperature convection heat transfer equation, as shown in Figure F.4. When predicting heat transfer with the discharge temperature form of the convective heat transfer equation, it is important that the corresponding constant c is used.
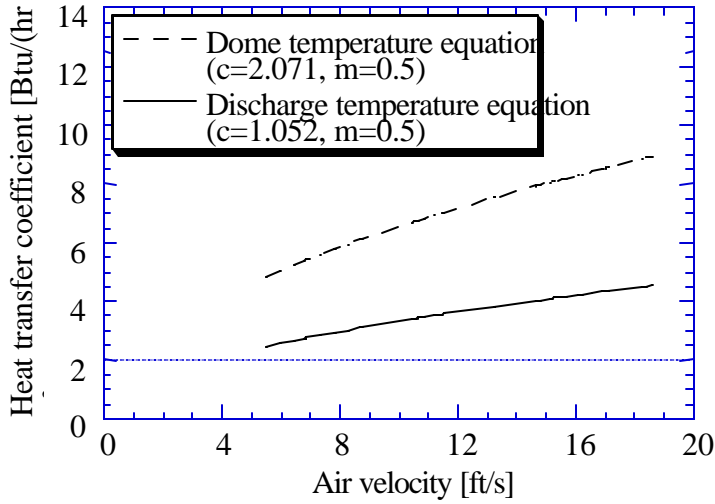
Figure F.4 Heat transfer coefficients bases on dome and discharge temperatures

In Figure F.5, the discharge temperature form of the convective heat transfer equation predicts heat transfer less accurately than by using the shell temperature. As a matter of fact, the precision interval is 56.7 Btu/hr when using the discharge temperature, while it is only 20.8 Btu/hr when using the dome temperature.
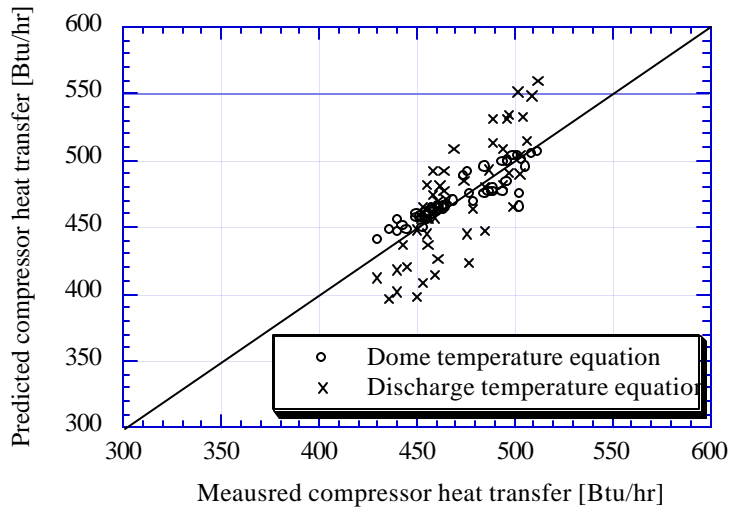

Figure F.5 Convective heat transfer based on dome and discharge temperatures

F.4 Estimating parameters from the rating point

While the power and refrigerant mass flow rate maps are for the tested Tecumseh AE1390V compressor (mounted on the Amana TC18MBL), the only available rating point conditions are for a compressor similar in size, the AE1420. These conditions specify air and suction temperatures of 90°F, condensing and evaporating temperatures of respectively 130 and -10°F. Under those conditions, the discharge temperature is 200°F. No information is given regarding the air velocity over the compressor, which is assumed to be at the nominal fan speed. Also, no information is given regarding the dome temperature of the compressor.

As found in Figure F.6, the relationship between discharge and dome temperature is linear for this compressor. For the 48 points of the Fall '93 data set, the two-parameter curve fit between dome and discharge temperatures is

$$T_{dome} = 0.855 \cdot T_{dis} - 24.7 \qquad\qquad (F.7)$$

where the units are in degrees Fahrenheit. Normally a modeler would not have available such extensive data to estimate these two parameters, but the discharge and dome temperatures at two operating conditions would be sufficient.

Often manufacturers provide dome temperature and discharge temperature at the rating point. Then a single-parameter linear fit through the origin might be a fair approximation. Since the manufacturer did not determine the dome temperature for this compressor, a dome temperature of 146.3°F is used for the corresponding discharge temperature of 200°F, as shown in Figure F.6. A single-parameter linear fit between this dome and discharge temperatures is

$$T_{dome} = 0.731 \cdot T_{dis} \qquad\qquad (F.8)$$
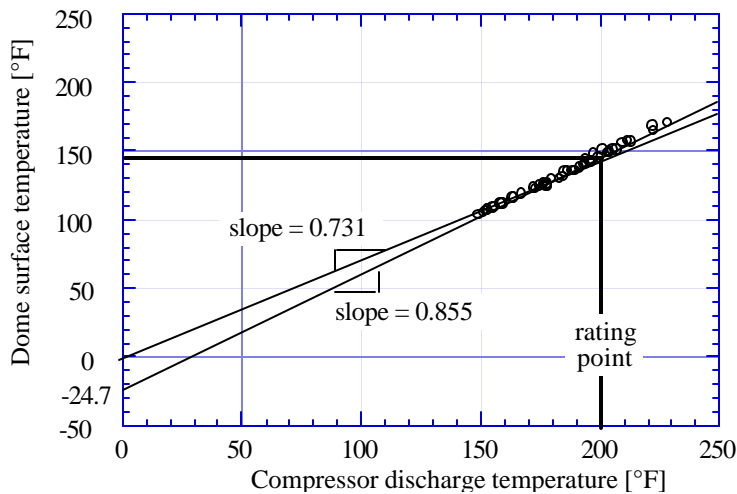
where the units are in degrees Fahrenheit.

Figure F.6 Relationship between discharge and shell temperature

At the rating point conditions, the constant c of the convective heat transfer equation is estimated by setting the exponent m = 0.5 and using the dome or discharge temperature, as shown in Table F.2. The result is only 2.5% higher than the value estimated earlier from the entire data set. Inaccuracies in the rating point discharge temperature and air velocity would affect the estimation of the parameter c.

Table F.4 Heat transfer coefficient parameters using rating point conditions

	c	m	Precision interval of Q_{comp} [Btu/hr]
Two-parameter fit of dome temperature	2.121	0.5	26.7
Single-parameter fit of dome temperature	2.121	0.5	81.7
Discharge temperature convective equation	1.086	0.5	74.3

The precision interval for estimating convective heat transfer depends mainly on whether the single-parameter or the two-parameter equations are used to relate the dome and discharge temperature. Table F.2 shows that using the single-parameter fit of the dome temperature deteriorates the precision interval as much as using the discharge temperature. Dome temperature is the theoretically correct way of describing convective heat transfer, so it should be used compared to the discharge temperature.

If adequate data are available, however, using the two-parameter fit of the dome temperature can significantly improve the precision interval. If compressor manufacturers would report both the dome and discharge temperatures at only one additional point to the rating point, a new and improved way of modeling compressors could be introduced. This additional information, which could be recorded while testing for power and mass flow rate maps, would not require much additional effort.

For the convective heat transfer correlation based on rating point conditions, the air-side heat transfer coefficient is $7.73 \frac{Btu}{hr\, ft^2\, °F}$ at the nominal fan speed, while Rubas and Bullard (1993) estimated a heat transfer coefficient of $7.85 \frac{Btu}{hr\, ft^2\, °F}$. This agreement is fairly good realizing that Rubas and Bullard (1993) did not have the same calorimeter setup as for the Spring '94 data set.

F.5 Modeling of the compressor

A simulation model of the compressor should be able to predict power required, heat loss, and outlet conditions, given only refrigerant and air inlet conditions and mass flow rates. The equations solved simultaneously in the model are refrigerant flow rate and input power compressor maps, first-law energy balance, and convective heat transfer equations.

Several approaches have been described earlier for determining the heat transfer coefficient of the compressor. The two-parameter fit of the dome temperature is chosen for the model, since it gave the best results. The results are compared to those obtained from the discharge temperature convective heat transfer equation of the type used by ADL (1982), and Merriam et al. (1993).

Given mass flow rate and inlet conditions, the mass flow rate map estimates the discharge pressure, as shown in Figure F.7, while the power map estimates the input power to the compressor, as shown in Figure F.8. The estimated condensing pressure is up to 80 psi higher than measured due to the propagation of errors of the mass flow rate map. As described in Appendix E: small errors in the mass flow rate map will produce large errors in condensing pressure.

The propagation of error in condensing pressure affects the compressor power predictions despite the fact that, as shown Appendix E, the compressor power map agrees well with the measured values. However when the discharge pressure estimated from the mass flow rate map is used in Figure F.8, the predicted compressor power is 10% larger than measured.

In Figures F.9 and 10, heat loss and discharge temperature are predicted as well. Although, the heat transfer correlation is estimated by producing the best agreement between predicted and measured heat transfer, the inaccuracy introduced by the map equations skew the heat transfer and discharge temperature results of the model.
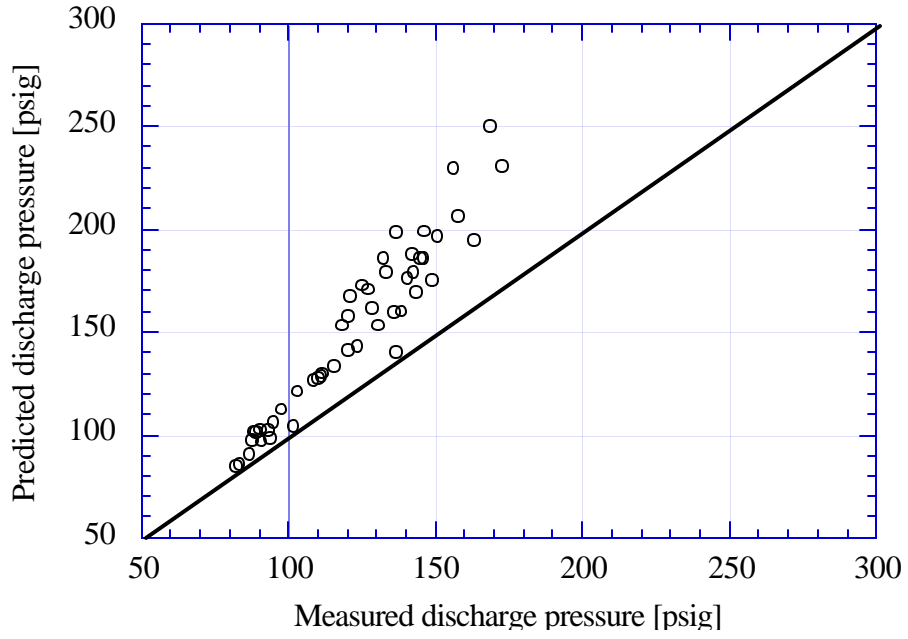
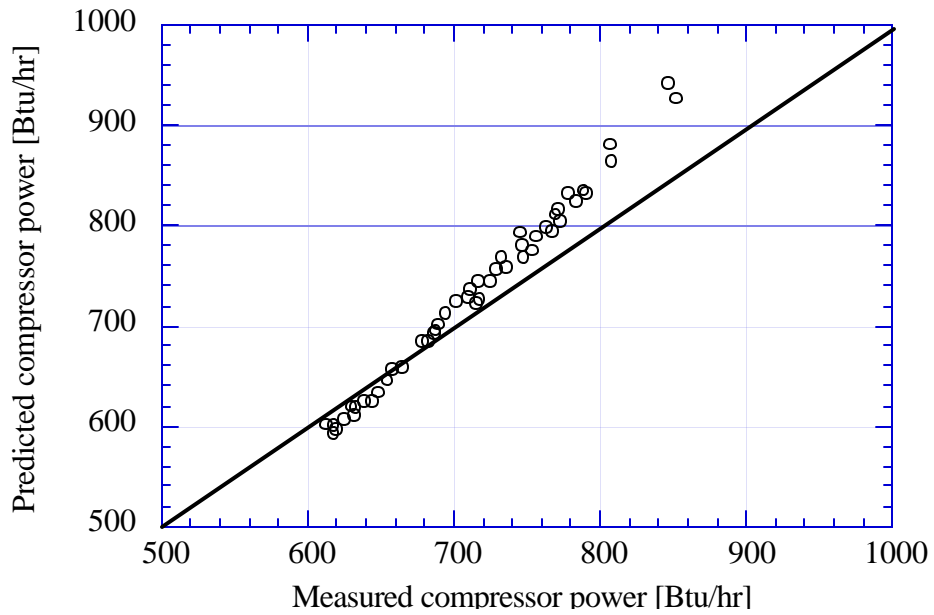Figure F.7 Condensing pressure with compressor model

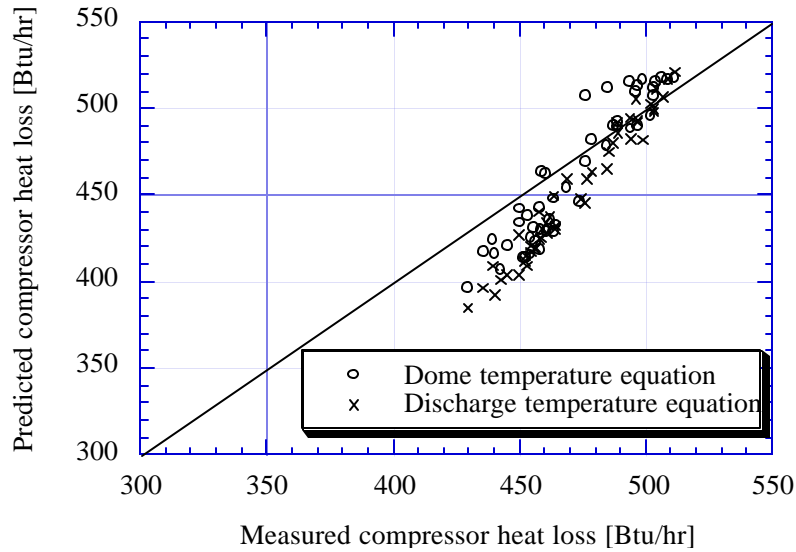Figure F.8 Input power with compressor model

Figure F.9 Convective heat transfer with compressor model
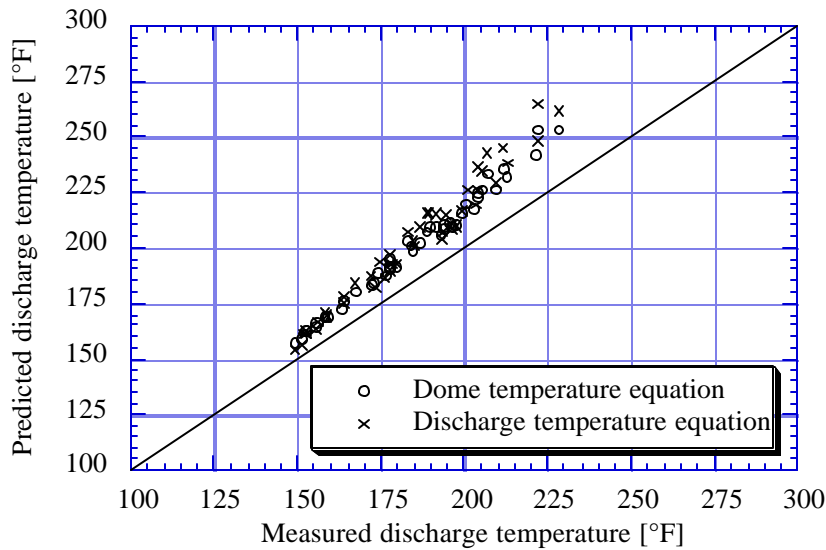
Figure F.10 Discharge temperature with compressor model

References

Arthur D. Little, Inc. *Refrigeration and Freezer Computer Model User's Guide*, U.S. Department of Energy, Washington D.C., 1982.

Icropera, F. P., and De Witt, D. P., *Fundamentals of Heat and Mass Transfer*, 3rd ed., John Wiley & Sons, Inc., New York, 1990.

Merriam, Richard, Varone, A., and Feng, H., EPA *Refrigerator Analysis Program User Manual,* Version 1.0, Arthur D. Little, Inc., 1993.

Rubas, P.J., and Bullard C.W., *Assessment of Factors Contributing to Refrigerator Cycling Losses*, ACRC TR-45, Air Conditioning and Refrigeration Center, University of Illinois at Urbana-Champaign, 1993.

Appendix G: Compressor second law analysis

G.1 Parameter estimation

This Appendix documents an unsuccessful attempt to use availability and second law analysis to predict compressor heat loss. The irreversibility (availability destruction) for the control volume is given by

$$I = Pwr_{comp} + \dot{m}_{ref} (a_{suc} - a_{dis}) \tag{G.1}$$

where I is the irreversibility, P_{comp} is the power delivered to the compressor, and a_{suc} and a_{dis} are respectively the suction-inlet and discharge-outlet availability. The control volume is around the compressor, therefore the availability of the heat transfer to the ambient is equal to zero.

Irreversibility is calculated from the availability balance using the inlet and outlet conditions, refrigerant flow rates, and power measurements from the complete Fall '93 data set. The heat loss was calculated directly from energy balance of the compressor.
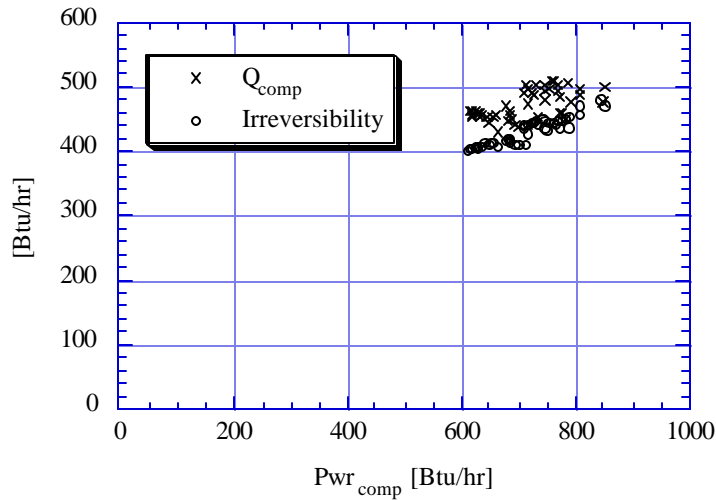

Figure G.1 Heat loss and irreversibility of the compressor

Figure G.1 shows that the heat loss generally exceeds the magnitude of the irreversibility. Physically, this might indicate a situation where all irreversibilities are dissipated as heat into the compressor shell (and thence into the air), while the gas is compressed in a nearly isentropic manner, and then cooled to T_{dis} as heat is transferred to the compressor shell:

$$Q_{comp} = I + \delta q \tag{G.2}$$

where the parameter δq is the difference in energy. This δq parameter should be equal to 0. Unfortunately, the availability analysis was unsuccessful in predicting the heat transfer of the compressor. A successful estimation of the parameter δq would allow to determine the heat loss in a simulation program.

Among numerous curve fits tried to estimate the δq parameter, the only successful one makes use of the difference between isentropic and actual discharge temperature.
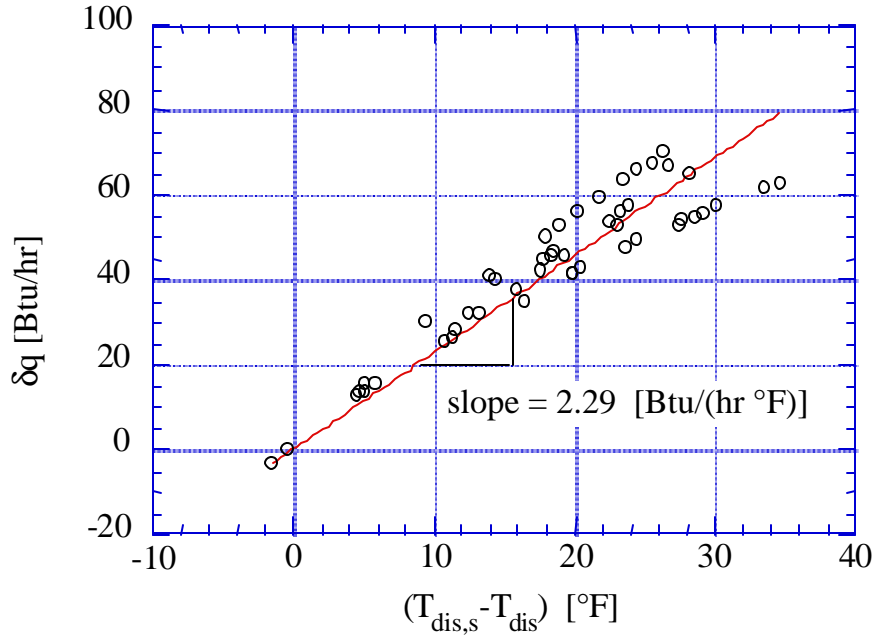
Figure G.2 δq for difference in isentropic to actual discharge temperatures

In figure G.2, this difference in temperature is directly proportional to the parameter δq. The fit goes through the origin and therefore can be represented only with the slope. All 48 data points of the data set were used, but to calculate the slope it is only required to use one point which could be the rating point of a compressor. In such case, it would be possible to model the compressor approximately without having to test it.

Heat loss is now rewritten as

$$Q_{comp} = I + 2.29 \ (T_{dis,s} - T_{dis}) \hspace{4cm} (G.3)$$

where $T_{dis,s}$ and T_{dis} are respectively the isentropic and actual discharge temperature. Figure G.3 is the successful display of the parameter estimation against the measured heat loss.
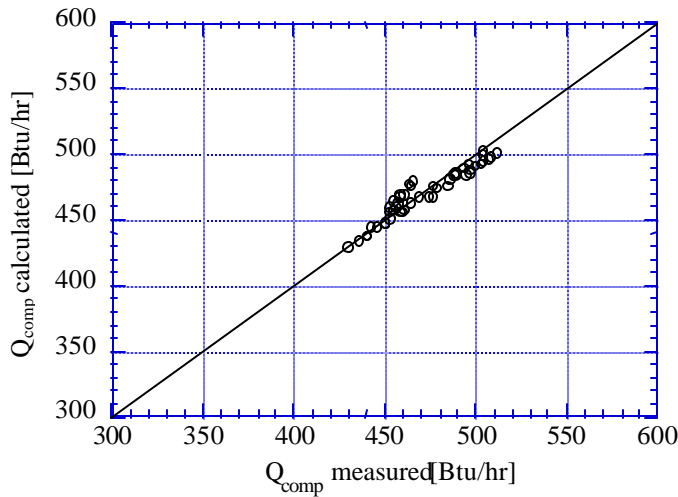

Figure G.3 Calculated and measured convective heat transfer

G.2 Compressor model

After proving the validity of the parameter estimation, the next step was to develop a simulation where only inlet conditions and refrigerant flow rates are given. The simulation solved several equations simultaneously. The set of equations include Equations G.1, G.3, an energy balance, and power and flow rate maps.

Unfortunately this model did not converge to specified tolerance. The numerical result for all of the data points were trivial solutions. That is, the discharge temperature of the compressor was equal to the isentropic discharge temperature. Even when the slope was set equal to zero in one of the runs, the model still gave the same type of answers. A possible explanation is that making use of availability, the parameter estimation Equation G.3, which is very similar to the second law, and energy makes the set of equations indefinite. As a matter of fact availability analysis is made up of both first and second law.

Appendix H: AC variable speed motor controller

H.1 Variable motor speed

The condenser fan is operated by an AC-shaded-four-pole Morrill motor. Specifications of this motor, as listed in Table 1, agree with experimental measurements except for the motor speed which is 1520 RPM. A stroboscope and the Hall-effect digital switch circuit described in Appendix I were used to measure motor speed.

Table H.1 Morrill motor specification

Rated output [Watt]	Nominal Speed [RPM]	Voltage [ACV]	Current [A]	Shaft Diameter [in]	Class
2	1300 CW	115	0.18	1/4	B

To control the speed of this type of motor in a linear way it is necessary to use an AC inverter and vary the frequency of the input voltage. Other alternatives were considered, as replacing the motor with a DC motor or with a Universal type motor and then varying the input voltage, but these new motors are much larger and could possibly influence flow dynamics and heat transfer.

A frequency controller is a non intrusive approach of varying fan speed. As a matter of fact, it is external to the experimental facility. Unfortunately, the motor had to be replaced because the higher speeds required a higher power rating to overcome the pressure drop across the condenser cabinet.

The fan laws state

$$CFM \propto D^3 \cdot RPM \tag{H.1}$$

and

$$HP \propto D^4 \cdot CFM^3 \cdot \rho \tag{H.2}$$

where CFM is air flow rate, D is the diameter of the fan, RPM is the motor speed, and HP is the horse power requirement. Therefore, air flow rate and motor speed are directly proportional to each other, and horsepower is proportional to flow rate to the third power. Consequently, to achieve desired flow rates 1.5 times larger than the nominal one, the original motor was replaced with a similar Morrill Motor described in Table H.2. The shape size of this new motor are identical and will not affect flow dynamics and heat transfer.

Table H.2 Morrill motor replacement specifications

Rated output [Watt]	Nominal Speed [RPM]	Voltage [ACV]	Current [A]	Shaft Diameter [in]	Class
6	1300 CW	115	0.18	1/4	B

H.2 Controller schematic

This circuit has evolved from the schematic of a variable speed turntable, with a basic concept of an oscillator that generates the signal and an amplifier that boost the signal to the motor, as shown in Figure H.1.
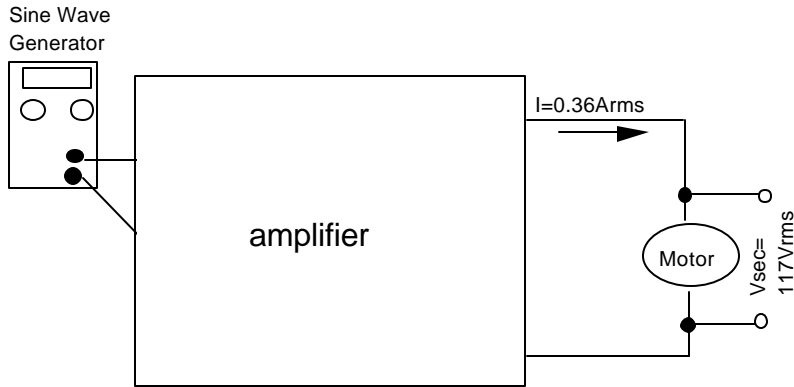
Figure H.1 Concept of AC motor controller concept

A lab sign wave generator is used for the oscillator, while the amplifying circuit is developed in the most cost efficient way. The final circuit, which shown in Figure H.2, is made up of two PA12 amplifiers that are in a quasi-parallel configuration. That is, the first amplifier amplifies the signal to the required voltage with the gain dictated by the feedback resistance, while the second amplifier acts as a follower to the output voltage of the first amplifier. Both amplifiers contribute equally to the current that drives the motor. It is true that having two amplifiers in parallel is not as simple as having one larger amplifier that runs the motor, but in this case it was cheaper to buy two PA12 rather than the larger PA04, which uses MOSFET technology and is virtually indestructible.
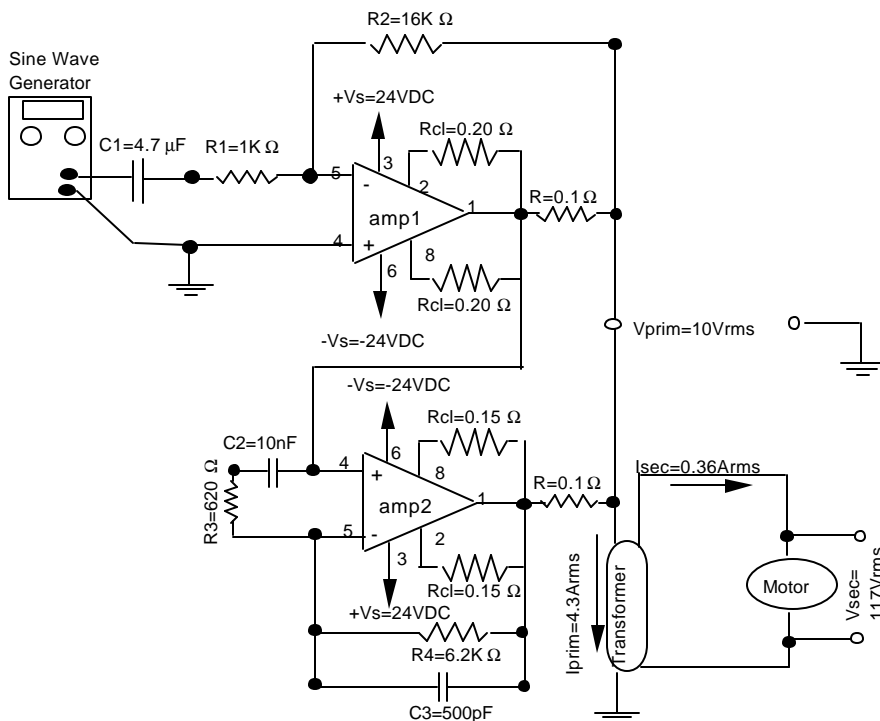

Figure H.2 Motor controller specifications

The input voltage to the amplifier goes through a passive filter that eliminates any DC offset. This filter is made up of capacitor C1 and resistor R1. The problem caused by any DC offset is that it will drive the output toward one of the rails and cause current and voltage limiting problems.

The output of the amplifiers is of 10 V and 4.3 A rms. Then the transformer steps up the voltage to 117 V to drive the motor. It is true that a transformer has energy losses and it would be preferable to drive the motor straight from the amplifier, but an amplifier with the same voltage and current specifications could not be found. High voltage amplifiers have high voltage ratings that vary between 200 to 300 volts, but have a low current output that needs to be stepped up. Power amplifiers, on the other hand, have lower voltage output, but much higher current capability that need to be stepped down. Because of the availability of other components, the power amplifier approach was chosen.

The PA 12 is a very high output current operational amplifier designed to drive resistive, inductive and capacitive loads. The amplifier's voltage and current specifications are listed in Table H.3 (Apex 1991).

Table H.3 Maximum ratings

Supply voltage +Vs to -Vs	100 V
Output current	15 A
Power dissipation	125 W
Voltage swing	Vs - 6

The amplifier must also be able to run within a SOA (safety operating area). The different limitations that make up the SOA curve are current handling capability, internal power dissipation capability, and heat sinking and secondary breakdown due to simultaneous hi collector-emitter voltage and high collector current.

Load is equally distributed between the two amplifiers with a peak current of 3 A per amplifier. The SOA is determined by calculating the supply to output voltage differential during peak current. With a phase shift of 53 degrees due to the nature of the inductive load, the differential voltage between supply and output is of 36 V. Assuming a resistive load would have given only a differential voltage of 28 V. For these operating conditions a HS05 heat sink must be used, any smaller heat sink would cause thermal runaway. Additional cooling with a fan will increase the thermal safety margin and the life of the amplifier.

H.3 Amplifying stability

When capacitive and inductive elements in the circuit resonate the amplifier encounters stability problems. This phenomenon is common in low gain configurations, with high currents and capacitive loads. The first amplifier has a large enough gain that it is virtually stable without any compensation, but the second amplifier that acts as a follower needs compensation to operate under stable conditions.

There are different approaches to determine the magnitude of these compensating elements. In this particular circuit, there are two compensating elements, the first one is the R-C circuit at the input of the second amplifier, while the second one is the R-C circuit in the feedback of the amplifier.

One way of determining analytically the stability of the circuit is to simulate the follower amplifier with the Spice circuit package. There are two approaches to model an amplifier: one specifies all of the diodes and transistors

in the amplifier while the other uses a dependent voltage source to simulate the amplifier and an R-C circuit to simulate the open loop gain. The more simplistic approach shown in Figure H.3 with the dependent voltage source is used, since the other approach is far more complicated.
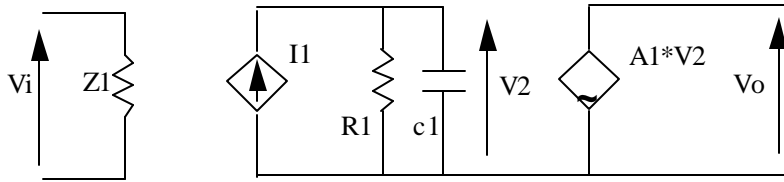

Figure H.3 AC linear model for amplifier

In Figure 3 , the break frequency is defined by the equation

$$fb = \frac{1}{2 \cdot \pi \cdot R1 \cdot C1}$$
(H.3)

and the open loop gain of the amplifier is defined by the equation

$$Ao = A1 \cdot R1$$
(H.4)

The Apex handbook (1991) specifies a break frequency of 100 Hz and a open loop gain of 110 Db. Thus, by picking the resistance R1 to be 10kΩ the capacitance C1 is 0.1593 µF, the gain A1 is 0.011 and the current I1 is equal to the input voltage Vi.

The model and the Apex consultant predicted that a capacitance of 10pF for C3 would be feasible. Unfortunately this model and the consultant were not right since the actual circuit turned out unstable.

With a workbench method it was later determined that a capacitance of at least 500 pF was required for stability. The workbench method is a trial and error approach where different values of capacitance were tested for C3. One of the factors that probably causes instability and cannot be modeled are large currents in the circuit that can cause the wires and the ground to act as capacitors. From the workbench method it was found that a much larger capacitance is needed, which trades off with the gain bandwidth capability of the circuit. Fortunately for this application it is not a problem since this circuit operates at very low frequencies.

Figure H.5 is a graphical representation that shows how by increasing capacitance it is possible to modify where Vo/Vi crosses the 0 Db line and consequently compensate the circuit. Ao is the open loop gain, 1/B is the feedback, and Vo/Vi is the closed loop.
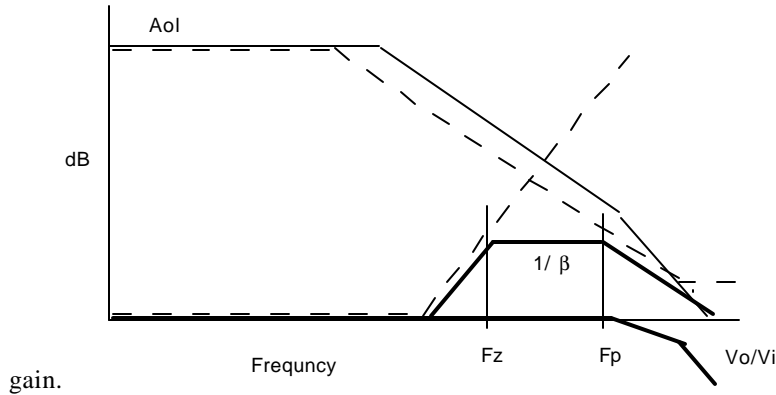
Figure H.5 Compensation by graphical method

The pole Fp can be calculated with the equation

$$Fp = \frac{1}{2 \cdot \pi \cdot C3 \cdot R4}$$
(H.5)

Increasing the capacitance C3 will move the pole Fp and crossing of the 0 Db line further to the left before the phase shift is above 180 degrees.

The other capacitance C2 dictates the position of the pole Fz. The frequency Fz is calculated with the equation

$$Fp = \frac{1}{2 \cdot \pi \cdot C2 \cdot R3}$$
(H.6)

Increasing C2 will also move the pole Fz further to the left. This pole has to be always farther to the left than Fp.

With a capacitance of 500 pF for C3, rather than the suggested 10pF, the pole Fp is 51 KHz. With a capacitance of 10nF for C2, as suggested from the consultant, the pole Fz is 25.5 Hz and smaller then the Fz.

H.4 Current Limiting

One of the features of the PA12 is the current limiting protection of the amplifier with the resistors Rcl. Each resistor and its power dissipation is calculated with the following equations

$$Rcl = \frac{0.65}{I_{lim}} - 0.01$$
(H.7)

$$Pcl = 0.65 \cdot I_{lim}$$
(H.8)

where 0.01 is accounts for wire bond and pin resistance. The limiting resistors are 0.20Ω for the first amplifier, while 0.15Ω for the second amplifier. The ohmmeter is not sensitive enough to measure such small resistances, therefore the nominal values on the resistors must be trusted.

H.5 Spice program listing

```
·     of ac motor inverter controller
·     voltage input
.AC    dec    10    .2HZ   2000000.2HZ
VIN    1    0    AC    10
·     components of input impeadence
R1    4    2    620
```

```
Ri    1    3    200M
C1    1    4    10nF
Ci    3    2    2pF
·     feedback loop
RF    2    5    6.2K
CF    3    5    10pF
·     load components
RR    5    6    0.1
RL    6    0    3.33
·     calling AMP
XA1   1    2    5    0 OPAMP
·     Op-amp subcircuit defenition
.SUBCKT OPAMP   1    2    7    4
RI    1    2    2.0E6
·     voltage controller current source with a gain of 1
GB    4    3    1    2    1
R1    3    4    10000
C1    3    4    0.1593uF
·     voltage controller voltage source with a gain of 11
EA    4    5    3    4    0.011
RO    5    7    75
·     end of subscript OPAMP
.ENDS OPAMP
.PLOT AC VM(6) VP(6)
.PROBE
.END
```

References

Apex Microtechnology Coorporation, *Apex Hybrid & IC Handbook*, Volume 5, Tucson, AZ, 1991.

Appendix I: Fan speedometer

A simple and cheap circuit setup is used to measure the motor speed of the evaporator and condenser fans, as shown in Figure I.1. The circuit is made up of a Hall-effect digital switch which by sensing a magnetic field sends a pulse (UGN3019T), a Shmitt Trigger that cleans up the signal (7414N), and a CMOS integrated circuit which converts the pulses to a square wave (DM74LS74AN). Then the signal is sent to an oscilloscope where the frequency is measured and converted to RPM.

The hall effect device is mounted directly on the fan, but the rest of the circuit is located outside the experimental facility. It is then possible to connect the Hall-effect switch on either the evaporator or condenser fans depending on what is needed for the experimental procedure.
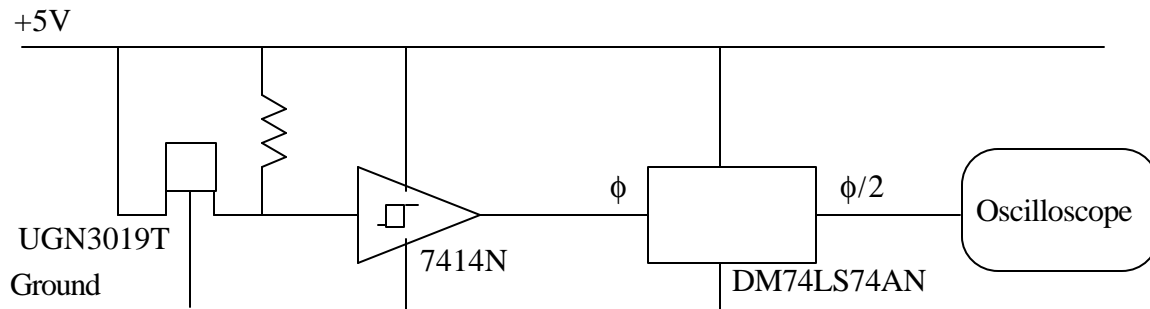

Figure I.1 Odometer schematic

A little refrigerator magnet which is mounted on the fan hub triggers the Hall-effect device every revolution. A second magnet is mounted on the radially opposite side of the hub to balance the fan. Since this second magnet is mounted with an opposite polarity facing the Hall-effect switch, it does not trigger the device.

A frequency-to-voltage converter would eliminate the need of an oscilloscope and the Strawberry Tree data acquisition system could directly record the motor speed of the fan. This would be worthwhile modification for further variable fan speed testing.